

Gaussian Process-Based Learning Control of Underactuated Balance Robots with an External and Internal Convertible Modeling Structure

Feng Han, Jingang Yi*

Department of Mechanical and Aerospace Engineering
Rutgers, The State University of New Jersey
Piscataway, NJ 08854, USA
Email: {fh233, jgyi}@rutgers.edu

External and internal convertible (EIC) form-based motion control is one of the effective designs of simultaneously trajectory tracking and balance for underactuated balance robots. Under certain conditions, the EIC-based control design however leads to uncontrolled robot motion. We present a Gaussian process (GP)-based data-driven learning control for underactuated balance robots with the EIC modeling structure. Two GP-based learning controllers are presented by using the EIC structure property. The partial EIC (PEIC)-based control design partitions the robotic dynamics into a fully actuated subsystem and one reduced-order underactuated system. The null-space EIC (NEIC)-based control compensates for the uncontrolled motion in a subspace, while the other closed-loop dynamics are not affected. Under the PEIC- and NEIC-based, the tracking and balance tasks are guaranteed and convergence rate and bounded errors are achieved without causing any uncontrolled motion by the original EIC-based control. We validate the results and demonstrate the GP-based learning control design performance using two inverted pendulum platforms.

1 Introduction

An underactuated balance robot possesses fewer control inputs than the number of degrees of freedom (DOFs) [1, 2]. Motion control of underactuated balance robots requires both the trajectory tracking of the actuated subsystem and balance control of the unactuated, unstable subsystem [3–5]. Inverting the non-minimum phase unactuated nonlinear dynamics brings additional challenges in causal feedback control design. Several modeling and control methods have been proposed for these robots and their applications [4–10]. Orbital stabilization method was used for balancing underactuated robots [11–13] with applications to bipedal robot [14] and cart-inverted pendulum [1]. A virtual constraint encoded the motion coordination between the actuated and unactuated subsystems. Energy shaping-based control was also de-

signed for underactuated balance robots in [15, 16]. One feature of those methods is that the achieved balance-enforced trajectory is not unique and cannot be prescribed explicitly [1, 11]. In [5, 17], a simultaneous trajectory tracking and balance control of underactuated balance robots was proposed by using the property of the external and internal convertible (EIC) form of the robot dynamics. The EIC-based control has been demonstrated as one of the effective approaches to achieve fast convergence and guaranteed performance that avoids non-causal continuous feedback control.

All of the above-mentioned control designs require an accurate model of robot dynamics and the control performance would deteriorate under model uncertainties or external disturbances. Machine learning-based methods provide an efficient tool for robot modeling and control. In particular, Gaussian process (GP) regression is an effective learning approach that generates nearly-analytical structure and bounded prediction errors [7, 18–20]. Development of GP-based performance-guaranteed control for underactuated balance robots has been reported [4, 18, 21]. In [4], the control design was conducted into two steps. A GP-based inverse dynamics controller for unactuated subsystem to achieve balance and a model predictive control (MPC) was used to simultaneously track the given reference trajectory and estimate the balance equilibrium manifold (BEM). The GP prediction uncertainties were incorporated into the control design to enhance the control robustness. The work in [5] followed the sequential control design in the EIC-based framework and the controller was adaptive to the prediction uncertainties. The training data was selected to reduce the computational complexity.

This paper takes advantage of the structured GP modeling approach in [5, 7] and presents an integration of EIC-based control with GP models. It is first shown that under certain conditions, there exist uncontrolled motions with the EIC-based control and this property can cause the entire system unstable. We identify these conditions and design the stable GP-based learning control with the properly selected

*Address all correspondence to J. Yi.

nominal robot dynamic model. Two different controllers, called partial- and null-space-EIC (i.e., PEIC- and NEIC), are presented to improve the performance of the EIC-based control. The PEIC-based control constructs a virtual inertial matrix to re-shape the dynamics coupling interactions between the actuated and unactuated subsystems. The EIC-induced uncontrolled motion is eliminated and the robotic system behaves as a combined fully actuated subsystem and a reduced-order unactuated subsystem. Alternatively, the compensation effect in NEIC-based control is applied to the uncontrolled coordinates in the null space, while the other part of the stable system motion stays unchanged. The PEIC- and NEIC-based controls achieve guaranteed robust performance with a fast convergence rate.

The main contribution of this work lies in the new GP-based learning control of underactuated balance robots using the EIC structural properties. Compared with the approaches in [5, 17], this work reveals underlying design properties and limitations of the EIC-based control for underactuated balance robots. We incorporate these discoveries into the GP-based data-driven modeling and learning control design. Such a GP-based control design has not been reported in previous work [4, 5, 7, 22, 23]. Compared with the work in [4, 23], the proposed method takes advantage of the attractive EIC modeling properties for control design and does not use MPC that requires highly computational demands. This paper is an extension of the previous conference submission [24] with new design, analyses and experiments. Particularly, the NEIC-based control design and experiments are new in this paper.

The rest of the paper is outlined as follows. We discuss the EIC-based control for underactuated balance robots and present the problem statement in Section 2. Section 3 presents the GP-based data-driven robot dynamics. The PEIC- and NEIC-based controls are presented in Section 4. The stability analysis is discussed in Section 5. The experimental results are presented in Section 6 and finally, Section 7 summarizes the concluding remarks.

2 EIC-Based Robot Control and Problem Statement

2.1 Robot Dynamics and EIC-Based Control

We consider an underactuated balance robot with $(n + m)$ DOFs, $n, m \in \mathbb{N}$, and the generalized coordinates are denoted as $\mathbf{q} \in \mathbb{R}^{n+m}$. The robot dynamics is expressed as

$$\mathbf{S} : \mathbf{D}(\mathbf{q})\ddot{\mathbf{q}} + \mathbf{C}(\mathbf{q}, \dot{\mathbf{q}})\dot{\mathbf{q}} + \mathbf{G}(\mathbf{q}) = \mathbf{B}\mathbf{u}, \quad (1)$$

where $\mathbf{D}(\mathbf{q})$, $\mathbf{C}(\mathbf{q}, \dot{\mathbf{q}})$ and $\mathbf{G}(\mathbf{q})$ are the inertial matrix, Coriolis, and gravity matrix, respectively. \mathbf{B} denotes the input matrix and $\mathbf{u} \in \mathbb{R}^n$ is the control input. The coordinates are partitioned as $\mathbf{q} = [\mathbf{q}_a^T \ \mathbf{q}_u^T]^T$, with actuated coordinate $\mathbf{q}_a \in \mathbb{R}^n$ and unactuated coordinate $\mathbf{q}_u \in \mathbb{R}^m$. We focus on the case $n \geq m$, and without loss of generality, we assume that $\mathbf{B} = [\mathbf{I}_n \ \mathbf{0}]^T$, where $\mathbf{I}_n \in \mathbb{R}^n$ is the identity matrix with dimension n . The

robot dynamic model in (1) is rewritten as

$$\mathbf{S}_a : \mathbf{D}_{aa}\ddot{\mathbf{q}}_a + \mathbf{D}_{au}\ddot{\mathbf{q}}_u + \mathbf{H}_a = \mathbf{u}, \quad (2a)$$

$$\mathbf{S}_u : \mathbf{D}_{ua}\ddot{\mathbf{q}}_a + \mathbf{D}_{uu}\ddot{\mathbf{q}}_u + \mathbf{H}_u = \mathbf{0} \quad (2b)$$

for actuated (\mathbf{S}_a) and unactuated (\mathbf{S}_u) subsystems, respectively. Subscripts “ aa (uu)” and “ ua and au ” indicate the variables related to the actuated (unactuated) coordinates and coupling effects, respectively. For presentation convenience, we introduce $\mathbf{H} = \mathbf{C}\dot{\mathbf{q}} + \mathbf{G}$, $\mathbf{H}_a = \mathbf{C}_a\dot{\mathbf{q}} + \mathbf{G}_a$, and $\mathbf{H}_u = \mathbf{C}_u\dot{\mathbf{q}} + \mathbf{G}_u$, and the dependence of \mathbf{D} , \mathbf{C} , and \mathbf{G} on \mathbf{q} and $\dot{\mathbf{q}}$ is dropped. Subsystems \mathbf{S}_a and \mathbf{S}_u are also referred to as the external and internal subsystems, respectively [4, 17].

The control goal is to steer actuated coordinate \mathbf{q}_a to follow a given desired trajectory \mathbf{q}_a^d for \mathbf{S}_a , while the unactuated, unstable subsystem \mathbf{S}_u is balanced at unknown equilibrium \mathbf{q}_u^e . Obtaining the estimate of \mathbf{q}_u^e needs to invert the non-minimum phase dynamics \mathbf{S}_u , which is challenging for non-causal control design.

The EIC-based control in [5, 17] first designs external input \mathbf{u} to follow \mathbf{q}_a^d by temporarily neglecting \mathbf{S}_u , namely,

$$\mathbf{u}^{\text{ext}} = \mathbf{D}_{aa}\mathbf{v}^{\text{ext}} + \mathbf{D}_{au}\ddot{\mathbf{q}}_u + \mathbf{H}_a, \quad (3)$$

where $\mathbf{v}^{\text{ext}} = \mathbf{q}_a^d - \mathbf{k}_{d1}\dot{\mathbf{e}}_a - \mathbf{k}_{p1}\mathbf{e}_a$ is the auxiliary input under which tracking error $\mathbf{e}_a = \mathbf{q}_a - \mathbf{q}_a^d$ converges to zero, $\mathbf{k}_{p1}, \mathbf{k}_{d1}$ are diagonal matrices with positive elements. To account for the coupling effect between \mathbf{S}_a and \mathbf{S}_u , the BEM is introduced as the equilibrium of \mathbf{q}_u under \mathbf{v}^{ext} , namely,

$$\mathcal{E} = \{\mathbf{q}_u^e : \mathbf{\Gamma}(\mathbf{q}_u; \mathbf{v}^{\text{ext}}) = \mathbf{0}, \dot{\mathbf{q}}_u = \ddot{\mathbf{q}}_u = \mathbf{0}\}, \quad (4)$$

where $\mathbf{\Gamma}(\mathbf{q}_u; \mathbf{v}^{\text{ext}}) = \mathbf{D}_{uu}\ddot{\mathbf{q}}_u + \mathbf{D}_{ua}\mathbf{v}^{\text{ext}} + \mathbf{H}_u$. \mathbf{q}_u^e is obtained by inverting $\mathbf{\Gamma}_0 = \mathbf{\Gamma}(\mathbf{q}_u; \mathbf{v}^{\text{ext}})|_{\dot{\mathbf{q}}_u=\ddot{\mathbf{q}}_u=\mathbf{0}} = \mathbf{0}$.

To stabilize \mathbf{q}_u onto \mathcal{E} , the control design updates \mathbf{q}_a balance motion as

$$\mathbf{v}^{\text{int}} = -\mathbf{D}_{ua}^+(\mathbf{H}_u + \mathbf{D}_{uu}\mathbf{v}_u^{\text{int}}), \quad (5)$$

where $\mathbf{D}_{ua}^+ = (\mathbf{D}_{ua}^T \mathbf{D}_{ua})^{-1} \mathbf{D}_{ua}^T$ is the generalized inverse of \mathbf{D}_{ua} , $\mathbf{v}_u^{\text{int}} = \mathbf{q}_u^e - \mathbf{k}_{d2}\dot{\mathbf{e}}_u - \mathbf{k}_{p2}\mathbf{e}_u$ is the auxiliary control that drives error $\mathbf{e}_u = \mathbf{q}_u - \mathbf{q}_u^e$ towards zero, and $\mathbf{k}_{p2}, \mathbf{k}_{d2}$ are diagonal matrices with positive elements. The final control is obtained by replacing \mathbf{v}^{ext} in (3) with \mathbf{v}^{int} in (5), that is,

$$\mathbf{u}^{\text{int}} = \mathbf{D}_{aa}\mathbf{v}^{\text{int}} + \mathbf{D}_{au}\ddot{\mathbf{q}}_u + \mathbf{H}_a. \quad (6)$$

Fig. 1(a) illustrates the above sequential EIC-based control design. It has been shown in [17] that the control \mathbf{u}^{int} guarantees both \mathbf{e}_a and \mathbf{e}_u convergence to a neighborhood of origin exponentially and therefore, the EIC-based control achieves trajectory tracking for \mathbf{S}_a and balancing task for \mathbf{S}_u simultaneously.

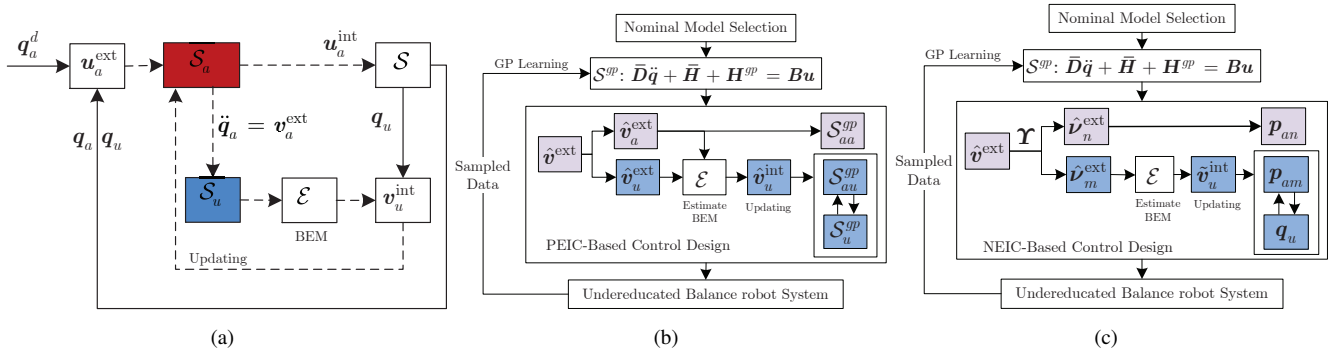


Fig. 1. Illustrative diagram of the control design for (a) the regular EIC-based control; (b) The PEIC-control design; and (c) the NEIC-based control design. In (a), the dashed line indicates the design flow and the solid line indicates the control flow.

2.2 Motion Property under EIC-based Control

Control design (5) uses a mapping from low-dimensional (m) to high-dimensional (n) space (i.e., $n \geq m$). Under control (6), it has been shown in [17] that there exists a finite time $T > 0$ and for small number $\varepsilon > 0$, $\|\mathbf{q}_u(t) - \mathbf{q}_u^e(t)\| < \varepsilon$ for $t > T$. Therefore, given the negligible error, we obtain $\mathbf{D}_{ua}(\mathbf{q}_a, \mathbf{q}_u) \approx \mathbf{D}_{ua}(\mathbf{q}_a, \mathbf{q}_u^e)$.

For \mathcal{S} in (2), if $\text{rank}(\mathbf{D}_{au}) = m$ for all \mathbf{q} , applying singular value decomposition (SVD) to \mathbf{D}_{ua} and \mathbf{D}_{ua}^+ , we have

$$\mathbf{D}_{ua} = \mathbf{U}\mathbf{\Lambda}\mathbf{V}^T, \quad \mathbf{D}_{ua}^+ = \mathbf{V}\mathbf{\Lambda}^+\mathbf{U}^T, \quad (7)$$

where $\mathbf{U} = [\mathbf{u}_1 \cdots \mathbf{u}_m] \in \mathbb{R}^{m \times m}$ and $\mathbf{V} \in \mathbb{R}^{n \times n}$ are unitary orthogonal matrices. $\mathbf{\Lambda} = [\mathbf{\Lambda}_m \mathbf{0}] \in \mathbb{R}^{m \times n}$, $\mathbf{\Lambda}^+ = [\mathbf{\Lambda}_m^{-1} \mathbf{0}]^T \in \mathbb{R}^{n \times m}$ and $\mathbf{\Lambda}_m = \text{diag}(\sigma_1, \dots, \sigma_m)$ with singular values $\sigma_i > 0$, $i = 1, \dots, m$. We partition \mathbf{V} into the block matrix $\mathbf{V} = [\mathbf{V}_m \mathbf{V}_n]$, $\mathbf{V}_m \in \mathbb{R}^{n \times m}$ and $\mathbf{V}_n \in \mathbb{R}^{n \times (n-m)}$. Since $\text{rank}(\mathbf{D}_{au}) = m$, the null space of \mathbf{D}_{ua} is $\ker(\mathbf{D}_{ua}) = \text{span}\{\mathbf{V}_n\}$.

Column vectors of matrix \mathbf{V} serve as a basis in \mathbb{R}^n and we introduce a coordinate transformation $\mathbf{\Upsilon}: \mathbf{x} \mapsto \mathbf{V}^T \mathbf{x}$ for $\mathbf{x} \in \mathbb{R}^n$. Clearly, $\mathbf{\Upsilon}$ is a linear, time-varying, smooth map. Applying $\mathbf{\Upsilon}$ to \mathbf{q}_a and \mathbf{v}^{ext} , we have

$$\mathbf{p}_a = \mathbf{V}^T \mathbf{q}_a, \quad \mathbf{v}^{\text{ext}} = \mathbf{V}^T \mathbf{v}^{\text{ext}}, \quad (8)$$

where $\mathbf{p}_a = [\mathbf{p}_{am}^T \mathbf{p}_{an}^T]^T$, $\mathbf{v}^{\text{ext}} = [(\mathbf{v}_m^{\text{ext}})^T (\mathbf{v}_n^{\text{ext}})^T]^T$, and $\mathbf{p}_{am}, \mathbf{v}_m^{\text{ext}} \in \mathbb{R}^m$, $\mathbf{p}_{an}, \mathbf{v}_n^{\text{ext}} \in \mathbb{R}^{n-m}$. Note that $[\mathbf{p}_a^T \mathbf{q}_u^T]^T$ still serves as a complete set of generalized coordinates for \mathcal{S} . Using the new coordinate \mathbf{p}_a , we have the following motion property under the EIC-based control for \mathcal{S} and the proof is given in Appendix A.1.

Lemma 1. For \mathcal{S} in (2), if $\text{rank}(\mathbf{D}_{au}) = m$ holds for \mathbf{q} and all n control inputs appear in \mathcal{S}_u dynamics (through $\ddot{\mathbf{q}}_a$), under the EIC-based control (6), the BEM \mathcal{E} in (4) is associated with only $\mathbf{v}_m^{\text{ext}}$ and robot dynamics can be written into

$$\mathcal{S}_{\text{EIC}}: \ddot{p}_{ai} = -\frac{\mathbf{u}_i^T (\mathbf{H}_u + \mathbf{D}_{uu} \mathbf{v}_u^{\text{int}})}{\sigma_i}, \quad i = 1, \dots, m, \quad (9a)$$

$$\ddot{p}_{aj} = 0, \quad j = m+1, \dots, n, \quad (9b)$$

$$\ddot{\mathbf{q}}_u = \mathbf{v}_u^{\text{int}}. \quad (9c)$$

No control input appears for coordinates in $\ker(\mathbf{D}_{ua})$ as shown in (9b) and only m actuated coordinates in $\text{span}(\mathbf{V})$ are under active control, as shown in (9a). The results in Lemma 1 reveal the motion property of the EIC-based control design. The uncontrolled motion happens to a special set of underactuated balance robots under the conditions in Lemma 1. If the unactuated motion is only related to m out of n control inputs, the motion (9b) vanishes and the EIC-based control works well. In [5], the EIC-based control worked properly for the rotary inverted pendulum with $n = m = 1$. In [4, 25], the EIC-based control also worked for the bikebot with $n = 2$ (planar motion) and $m = 1$ (roll motion) but the roll motion depends on steering control only, that is, no velocity control, and therefore, does not satisfy the condition for Lemma 1. We will show an example of the 3-link inverted pendulum platform that demonstrates the uncontrolled motion under the EIC-based control in Section 6.

With the above-discussed motion property under the EIC-based control, we consider the following problem.

Problem Statement: The goal of robot control is to design an enhanced EIC-based learning control to drive the actuated coordinate \mathbf{q}_a to follow a given profile \mathbf{q}_a^d and simultaneously the unactuated coordinate \mathbf{q}_u to be stabilized on the estimated profile \mathbf{q}_u^e using the GP-based data-driven model. The uncontrolled motion presented in Lemma 1 should be avoided for robot dynamics (2).

3 GP-Based Robot Dynamics Model

We build a GP-based robot dynamics model that will be used for control design in the next section.

3.1 GP-Based Robot Dynamics Model

To keep self-contained, we briefly review the GP model. We consider a multivariate continuously smooth function $y = f(\mathbf{x}) + w$, $\mathbf{x}_i \in \mathbb{R}^{n_x}$, where $w \in \mathbb{R}$ is the zero-mean Gaussian noise and n_x is the dimension of \mathbf{x} . Denote the training data as $\mathbb{D} = \{\mathbf{X}, \mathbf{Y}\} = \{\mathbf{x}_i, y_i\}_{i=1}^N$, where $\mathbf{X} = \{\mathbf{x}_i\}_{i=1}^N$, $\mathbf{Y} = \{y_i\}_{i=1}^N$, and $N \in \mathbb{N}$ is the number of the data point. The GP model is trained by maximizing posterior probability $p(\mathbf{Y}; \mathbf{X}, \boldsymbol{\Theta})$ over the hyperparameters $\boldsymbol{\Theta}$, that is, $\boldsymbol{\Theta}$ is obtained by solving

$$\min_{\boldsymbol{\Theta}} -\log(\mathbf{Y}; \mathbf{X}, \boldsymbol{\Theta}) = \min_{\boldsymbol{\Theta}} -\frac{1}{2} \mathbf{Y}^T \mathbf{K}^{-1} \mathbf{Y} - \frac{1}{2} \log \det(\mathbf{K}),$$

where $\mathbf{K} = (K_{ij})$, $K_{ij} = k(\mathbf{x}_i, \mathbf{x}_j) = \sigma_f^2 \exp(-\frac{1}{2}(\mathbf{x}_i - \mathbf{x}_j)^T \mathbf{W}(\mathbf{x}_i - \mathbf{x}_j)) + \vartheta^2 \delta_{ij}$, $\mathbf{W} = \text{diag}\{W_1, \dots, W_{n_x}\} > 0$, $\delta_{ij} = 1$ for $i = j$, and $\Theta = \{\mathbf{W}, \sigma_f, \vartheta\}$ are hyperparameters.

Given \mathbf{x}^* , the GP model predicts the corresponding y and the joint distribution is

$$\begin{bmatrix} \mathbf{Y} \\ y \end{bmatrix} \sim \mathcal{N}\left(\mathbf{0}, \begin{bmatrix} \mathbf{K} & \mathbf{k}^T \\ \mathbf{k} & k^* \end{bmatrix}\right), \quad (10)$$

where $\mathcal{N}(\boldsymbol{\mu}, \boldsymbol{\Sigma})$ denotes the Gaussian distribution with mean $\boldsymbol{\mu}$ and variance $\boldsymbol{\Sigma}$, $\mathbf{k} = \mathbf{k}(\mathbf{x}^*, \mathbf{X})$ and $k^* = k(\mathbf{x}^*, \mathbf{x}^*)$. The mean value and variance for input \mathbf{x}^* are

$$\mu_i(\mathbf{x}^*) = \mathbf{k}^T \mathbf{K}^{-1} \mathbf{Y}, \quad \Sigma_i(\mathbf{x}^*) = k^* - \mathbf{k} \mathbf{K}^{-1} \mathbf{k}^T. \quad (11)$$

For robot dynamics \mathcal{S} in (1), we first build a nominal model

$$\mathcal{S}^n : \bar{\mathbf{D}}\ddot{\mathbf{q}} + \bar{\mathbf{H}} = \mathbf{B}\mathbf{u}, \quad (12)$$

where $\bar{\mathbf{D}}$ and $\bar{\mathbf{H}}$ are the nominal inertia and nonlinear matrices, respectively. In general, the nominal dynamic model does not hold for the data sampled from the physical robot systems. The GP models are built to capture the difference between \mathcal{S}^n and \mathcal{S} , namely,

$$\mathbf{H}^e = \mathbf{D}\ddot{\mathbf{q}} + \mathbf{H} - \bar{\mathbf{D}}\ddot{\mathbf{q}} - \bar{\mathbf{H}} = \mathbf{B}\mathbf{u} - \bar{\mathbf{D}}\ddot{\mathbf{q}} - \bar{\mathbf{H}}.$$

We build GP models to estimate $\mathbf{H}^e = [(\mathbf{H}_a^e)^T (\mathbf{H}_u^e)^T]^T$, where \mathbf{H}_a^e and \mathbf{H}_u^e are for \mathcal{S}_a and \mathcal{S}_u , respectively. The training data $\mathbb{D} = \{\mathbf{X}, \mathbf{Y}\}$ are sampled from \mathcal{S} as $\mathbf{X} = \{\mathbf{q}, \dot{\mathbf{q}}, \ddot{\mathbf{q}}\}$ and $\mathbf{Y} = \{\mathbf{H}^e\}$.

The GP predicted mean and variance are denoted as $(\boldsymbol{\mu}_i(\mathbf{x}), \boldsymbol{\Sigma}_i(\mathbf{x}))$ for \mathbf{H}_i^e , $i = a, u$. The GP-based robot dynamics models \mathcal{S}_a^{gp} and \mathcal{S}_u^{gp} for \mathcal{S}_a and \mathcal{S}_u respectively are given as

$$\mathcal{S}_a^{gp} : \bar{\mathbf{D}}_{aa}\ddot{\mathbf{q}}_a + \bar{\mathbf{D}}_{au}\ddot{\mathbf{q}}_u + \mathbf{H}_a^{gp} = \mathbf{u}, \quad (13a)$$

$$\mathcal{S}_u^{gp} : \bar{\mathbf{D}}_{ua}\ddot{\mathbf{q}}_a + \bar{\mathbf{D}}_{uu}\ddot{\mathbf{q}}_u + \mathbf{H}_u^{gp} = \mathbf{0}, \quad (13b)$$

where $\mathbf{H}_i^{gp} = \bar{\mathbf{H}}_i + \boldsymbol{\mu}_i(\mathbf{x})$, $i = a, u$. The GP-based model prediction error is

$$\boldsymbol{\Delta} = \begin{bmatrix} \boldsymbol{\Delta}_a \\ \boldsymbol{\Delta}_u \end{bmatrix} = \begin{bmatrix} \boldsymbol{\mu}_a(\mathbf{x}) - \mathbf{H}_a^e \\ \boldsymbol{\mu}_u(\mathbf{x}) - \mathbf{H}_u^e \end{bmatrix}. \quad (14)$$

To quantify the GP-based model prediction error, the following property for $\boldsymbol{\Delta}$ is obtained directly from Theorem 6 in [26].

Lemma 2. *Given training dataset \mathbb{D} , if the kernel function $k(\mathbf{x}_i, \mathbf{x}_j)$ is chosen such that \mathbf{H}_a^e for \mathcal{S}_a has a finite reproducing kernel Hilbert space norm $\|\mathbf{H}_a^e\|_k < \infty$, for given $0 < \eta_a < 1$,*

$$\Pr\left\{\|\boldsymbol{\Delta}_a\| \leq \|\boldsymbol{\kappa}_a^T \boldsymbol{\Sigma}_a^{1/2}(\mathbf{x})\|\right\} \geq \eta_a, \quad (15)$$

where $\Pr\{\cdot\}$ denotes the probability of an event, $\boldsymbol{\kappa}_a \in \mathbb{R}^n$ and its i -th entry is $\kappa_{ai} = \sqrt{2\|\mathbf{H}_{a,i}^e\|_k^2 + 300\zeta_i \ln^3 \frac{N+1}{1-\eta_a^2}}$, $\zeta_i = \max_{\mathbf{x}, \mathbf{x}' \in \mathbf{X}} \frac{1}{2} \ln |1 + \vartheta_i^{-2} k_i(\mathbf{x}, \mathbf{x}')|$. A similar conclusion holds for $\boldsymbol{\Delta}_u$ with $0 < \eta_u < 1$.

3.2 Nominal Model Selection

The nominal model plays an important role in the EIC control. We consider the following conditions for choosing the nominal GP model \mathcal{S}^{gp} to overcome the uncontrolled motion that was pointed out in Lemma 1 under the learning control.

C_1 : $\bar{\mathbf{D}} = \bar{\mathbf{D}}^T$ is positive definite, $\|\bar{\mathbf{D}}\| \leq d$, $\|\bar{\mathbf{H}}\| \leq h$, where constants $0 < d, h < \infty$;

C_2 : $\text{rank}(\bar{\mathbf{D}}_{aa}) = n$, $\text{rank}(\bar{\mathbf{D}}_{uu}) = \text{rank}(\bar{\mathbf{D}}_{ua}) = m$; and

C_3 : non-constant kernel of $\bar{\mathbf{D}}_{ua}$.

With C_1 and C_2 , the generalized inverses of $\bar{\mathbf{D}}_{aa}$, $\bar{\mathbf{D}}_{uu}$, and $\bar{\mathbf{D}}_{au}$ exist, which are used to compute the auxiliary controls. We can select $\bar{\mathbf{D}} = \bar{\mathbf{D}}^T$ to ensure $\bar{\mathbf{D}}_{au} = \bar{\mathbf{D}}_{ua}^T$. To see the requirement of C_3 , we rewrite $\mathbf{q}_a = \sum_{i=1}^n p_{ai} \mathbf{v}_i$. By (9), under the updated control \mathbf{v}^{int} , $\ddot{\mathbf{q}}_a = \sum_{i=1}^n \ddot{p}_{ai} \mathbf{v}_i + \sum_{i=m+1}^n \ddot{p}_{ai} \mathbf{v}_i$, where \mathbf{v}_i is the i th column of \mathbf{V} . Note that the part $\sum_{i=m+1}^n \ddot{p}_{ai} \mathbf{v}_i$ of \mathcal{S}_a dynamics is free of control if \mathbf{V} is constant. In spite of the fact that \mathbf{q}_u stabilizes on \mathbf{q}_u^e , \mathbf{q}_a converges to \mathbf{q}_a^d only in an m -dimensional subspace and the other $(n-m)$ dimensional motion uncontrolled. If the system is stable, the uncontrolled motion cannot be fixed in the configuration space throughout entire control process. Therefore, a non-constant kernel $\bar{\mathbf{D}}_{ua}$ is needed.

Conditions C_1 - C_3 provide the sufficient control-oriented nominal model selection criteria. The commonly used nominal model in [5, 7] is $\bar{\mathbf{D}}\ddot{\mathbf{q}} = \mathbf{B}\mathbf{u}$ with $\bar{\mathbf{H}} = \mathbf{0}$. The constant nominal model is used in [7] as the system is fully actuated. It is not difficult to satisfy the above nominal model conditions in practice. First, the nonlinear term is canceled by feedback linearization and $\bar{\mathbf{H}} = \mathbf{0}$ can be used. Matrix $\bar{\mathbf{D}}$ captures the robots' inertia property. The mass and length of robot links are usually available or can be measured. Meanwhile, dynamics coupling for revolute joints shows up in the inertia matrix as trigonometric functions of the relative joint angles. Therefore, the diagonal elements can be filled with mass or inertia estimates and the off-diagonal entries can be constructed with trigonometric functions multiplying inertia constants. We will show model selection examples in Section 6.

4 GP-Enhanced EIC-Based Control

In this section, we propose two enhanced controllers using the GP model \mathcal{S}^{gp} , i.e., PEIC- and NEIC-based control. The PEIC-based control aims to eliminate uncontrolled motion under the EIC-based control, while the NEIC-based control directly manages the uncontrolled motion.

4.1 Robust Auxiliary Control

The control design should follow the guideline: (1) the \mathbf{p}_{am} and \mathbf{q}_u dynamics are preserved (since they are stable under the EIC-based control) and (2) the uncontrolled motion (in S_a^{gp}) is either eliminated or under active control. The second requirement also implies that the motion of the unactuated coordinates depends on only m control inputs. To see this, solving $\ddot{\mathbf{q}}_a$ from S_a^{gp} and plugging it into S_u^{gp} yields

$$(\bar{\mathbf{D}}_{uu} - \bar{\mathbf{D}}_{ua}\bar{\mathbf{D}}_{aa}^{-1}\bar{\mathbf{D}}_{au})\ddot{\mathbf{q}}_u + \mathbf{H}_u^{gp} - \bar{\mathbf{D}}_{ua}\bar{\mathbf{D}}_{aa}^{-1}\mathbf{H}_a^{gp} = -\bar{\mathbf{D}}_{ua}\bar{\mathbf{D}}_{aa}^{-1}\mathbf{u}.$$

Note that $\bar{\mathbf{D}}_{ua} \in \mathbb{R}^{m \times n}$, $\bar{\mathbf{D}}_{aa}^{-1} \in \mathbb{R}^{n \times n}$, and \mathbf{q}_u is overactuated given $n = \dim(\mathbf{u}) \geq m = \dim(\mathbf{q}_u)$. If \mathbf{q}_u depends on the same number of control inputs, $(n - m)$ column vectors in $\bar{\mathbf{D}}_{ua}\bar{\mathbf{D}}_{aa}^{-1}$ should be zero. Thus, the EIC-based control is applied between the same number of actuated and unactuated coordinates.

With S^{gp} , we update the predictive variance of S_a^{gp} into the auxiliary control \mathbf{v}^{ext} in (3) as

$$\hat{\mathbf{v}}^{\text{ext}} = \ddot{\mathbf{q}}_a^d - \hat{\mathbf{k}}_{p1}\mathbf{e}_a - \hat{\mathbf{k}}_{d1}\dot{\mathbf{e}}_a \quad (16)$$

where $\hat{\mathbf{k}}_{p1} = \mathbf{k}_{p1} + k_{n1}\boldsymbol{\Sigma}_a$ and $\hat{\mathbf{k}}_{d1} = \mathbf{k}_{d1} + k_{n2}\boldsymbol{\Sigma}_a$ are control gains with parameters $k_{n1}, k_{n2} \geq 0$. The variance of GP prediction $\boldsymbol{\Sigma}_a$ captures the uncertainty in robot dynamics and is updated online with sensor measurements.

Given the GP-based dynamics, the BEM is estimated by solving the optimization problem

$$\hat{\mathbf{q}}_u^e = \arg \min_{\mathbf{q}_u} \|\Gamma_0(\mathbf{q}_u; \hat{\mathbf{v}}^{\text{ext}})\|. \quad (17)$$

The updated control design is

$$\hat{\mathbf{v}}_u^{\text{int}} = \ddot{\mathbf{q}}_u^e - \hat{\mathbf{k}}_{p2}\dot{\mathbf{e}}_u - \hat{\mathbf{k}}_{d2}\dot{\mathbf{e}}_u, \quad (18)$$

where $\dot{\mathbf{e}}_u = \mathbf{q}_u - \hat{\mathbf{q}}_u^e$ is the internal system tracking error relative to the estimated BEM. Similar as $\hat{\mathbf{k}}_{p2}, \hat{\mathbf{k}}_{d2}$, $\hat{\mathbf{k}}_{p2} = \mathbf{k}_{p2} + k_{n3}\boldsymbol{\Sigma}_u$ and $\hat{\mathbf{k}}_{d2} = \mathbf{k}_{d2} + k_{n4}\boldsymbol{\Sigma}_u$ depend on $\boldsymbol{\Sigma}_u$ with the parameters by $k_{n3}, k_{n4} \geq 0$.

Let $\Delta\mathbf{q}_u^e = \mathbf{q}_u^e - \hat{\mathbf{q}}_u^e$ denote the BEM estimation error and the actual BEM is $\mathbf{q}_u^e = \hat{\mathbf{q}}_u^e + \Delta\mathbf{q}_u^e$. The control design based on actual BEM should be $\mathbf{v}_u^{\text{int}} = \ddot{\mathbf{q}}_u^e - \hat{\mathbf{k}}_{p2}\dot{\mathbf{e}}_u - \hat{\mathbf{k}}_{d2}\dot{\mathbf{e}}_u$ and therefore, we have

$$\mathbf{v}_u^{\text{int}} = \hat{\mathbf{v}}_u^{\text{int}} - \Delta\mathbf{v}_u^{\text{int}},$$

where $\Delta\mathbf{v}_u^{\text{int}} = \Delta\ddot{\mathbf{q}}_u^e + \hat{\mathbf{k}}_{p2}\Delta\dot{\mathbf{q}}_u^e + \hat{\mathbf{k}}_{d2}\Delta\dot{\mathbf{q}}_u^e$. Compared to (4), the BEM estimation error comes from GP modeling error and optimization accuracy. It is reasonable to assume that $\Delta\mathbf{q}_u^e$ is bounded. Because of the bounded Gaussian kernel function, the GP prediction variances are also bounded, i.e.,

$$\|\boldsymbol{\Sigma}_a(\mathbf{x})\| \leq (\sigma_a^{\max})^2, \|\boldsymbol{\Sigma}_u(\mathbf{x})\| \leq (\sigma_u^{\max})^2, \quad (19)$$

where $\sigma_a^{\max} = \max_i(\sigma_{fai}^2 + \vartheta_{ai}^2)^{1/2}$, $\sigma_u^{\max} = \max_i(\sigma_{fui}^2 + \vartheta_{ui}^2)^{1/2}$, σ_f and ϑ are the hyperparameters in each channel. Furthermore, we require the control gains to satisfy the following bounds

$$k_{i1} \leq \lambda(\hat{\mathbf{k}}_{i1}) \leq k_{i3}, \quad k_{i2} \leq \lambda(\hat{\mathbf{k}}_{i2}) \leq k_{i4}, \quad i = p, d$$

for constants $k_{pj}, k_{dj} > 0$, $j = 1, \dots, 4$, where $\lambda(\cdot)$ denotes the eigenvalue operator.

4.2 PEIC-Based Control Design

The control design \mathbf{v}^{int} in (5) updates the input \mathbf{v}^{ext} and \mathbf{q}_a then acts as a control input to steer \mathbf{q}_u to \mathbf{q}_u^e . The S_u dynamics is rewritten into

$$\ddot{\mathbf{q}}_u = -\mathbf{D}_{uu}^{-1}\mathbf{H}_u - \mathbf{D}_{uu}^{-1}\mathbf{D}_{ua}\ddot{\mathbf{q}}_a.$$

We instead consider the coupling effect between \mathbf{q}_a and \mathbf{q}_u and assign m control inputs for the unactuated subsystem. To achieve such a goal, we partition the actuated coordinates as $\mathbf{q}_a = [\mathbf{q}_{aa}^T \mathbf{q}_{au}^T]^T$, $\mathbf{q}_{aa} \in \mathbb{R}^m$, $\mathbf{q}_{au} \in \mathbb{R}^{n-m}$, and $\mathbf{u} = [\mathbf{u}_a^T \mathbf{u}_u^T]^T$. The S^{gp} dynamics in (13) is rewritten as

$$\begin{bmatrix} \bar{\mathbf{D}}_{aa}^a & \bar{\mathbf{D}}_{aa}^{au} & \bar{\mathbf{D}}_{au}^a \\ \bar{\mathbf{D}}_{aa}^{au} & \bar{\mathbf{D}}_{aa}^u & \bar{\mathbf{D}}_{au}^u \\ \bar{\mathbf{D}}_{ua}^a & \bar{\mathbf{D}}_{ua}^u & \bar{\mathbf{D}}_{uu} \end{bmatrix} \begin{bmatrix} \ddot{\mathbf{q}}_{aa} \\ \ddot{\mathbf{q}}_{au} \\ \ddot{\mathbf{q}}_u \end{bmatrix} + \begin{bmatrix} \mathbf{H}_{aa}^{gp} \\ \mathbf{H}_{au}^{gp} \\ \mathbf{H}_u^{gp} \end{bmatrix} = \begin{bmatrix} \mathbf{u}_a \\ \mathbf{u}_u \\ \mathbf{0} \end{bmatrix}, \quad (20)$$

where all block matrices are in proper dimensions. We rewrite (20) into three groups as

$$S_{aa}^{gp} : \bar{\mathbf{D}}_{aa}^a \ddot{\mathbf{q}}_{aa} + \mathbf{H}_{aa}^a = \mathbf{u}_a, \quad (21a)$$

$$S_{au}^{gp} : \bar{\mathbf{D}}_{aa}^u \ddot{\mathbf{q}}_{au} + \bar{\mathbf{D}}_{au}^u \ddot{\mathbf{q}}_u + \mathbf{H}_{au}^u = \mathbf{u}_u, \quad (21b)$$

$$S_u^{gp} : \bar{\mathbf{D}}_{ua}^u \ddot{\mathbf{q}}_{au} + \bar{\mathbf{D}}_{uu} \ddot{\mathbf{q}}_u + \mathbf{H}_{uu} = \mathbf{0}, \quad (21c)$$

where $\mathbf{H}_{aa}^a = \bar{\mathbf{D}}_{aa}^{au} \ddot{\mathbf{q}}_{au} + \bar{\mathbf{D}}_{au}^a \ddot{\mathbf{q}}_u + \mathbf{H}_{aa}^{gp}$, $\mathbf{H}_{au}^u = \bar{\mathbf{D}}_{aa}^u \ddot{\mathbf{q}}_{au} + \bar{\mathbf{D}}_{au}^u \ddot{\mathbf{q}}_u + \mathbf{H}_{au}^{gp}$, and $\mathbf{H}_{uu} = \bar{\mathbf{D}}_{ua}^u \ddot{\mathbf{q}}_{au} + \bar{\mathbf{D}}_{uu} \ddot{\mathbf{q}}_u + \mathbf{H}_u^{gp}$. Apparently, S_u^{gp} is virtually independent of S_{aa}^{gp} and the dynamics coupling exists only between S_{au}^{gp} and S_{aa}^{gp} .

Let $\hat{\mathbf{v}}^{\text{ext}}$ in (16) be partitioned into $\hat{\mathbf{v}}_a^{\text{ext}}$ and $\hat{\mathbf{v}}_u^{\text{ext}}$ corresponding to \mathbf{q}_{aa} and \mathbf{q}_{au} , respectively. $\hat{\mathbf{v}}_a^{\text{ext}}$ is directly applied to S^{gp} and $\hat{\mathbf{v}}_u^{\text{ext}}$ is updated for balance control purpose. As aforementioned, the condition to eliminate the uncontrolled motion in S_a is that \mathbf{q}_u only depends on m inputs. The task of driving \mathbf{q}_u to \mathbf{q}_u^e is assigned to \mathbf{q}_{au} coordinates only. With this observation, the PEIC-based control takes the form of $\hat{\mathbf{u}}^{\text{int}} = [\hat{\mathbf{u}}_a^T \hat{\mathbf{u}}_u^T]^T$ with

$$\hat{\mathbf{u}}_a = \bar{\mathbf{D}}_{aa}^a \hat{\mathbf{v}}_a^{\text{ext}} + \mathbf{H}_{aa}^a, \quad \hat{\mathbf{u}}_u = \bar{\mathbf{D}}_{aa}^u \hat{\mathbf{v}}_u^{\text{int}} + \bar{\mathbf{D}}_{au}^u \ddot{\mathbf{q}}_u + \mathbf{H}_{au}^u, \quad (22)$$

where $\hat{\mathbf{v}}_u^{\text{int}} = -(\bar{\mathbf{D}}_{ua}^u)^{-1}(\mathbf{H}_{uu} + \bar{\mathbf{D}}_{uu} \hat{\mathbf{v}}_u^{\text{int}})$. Clearly, the unactuated subsystem only depends on \mathbf{u}_u under the PEIC design. The following lemma presents the qualitative assessment of the PEIC-based control and the proof is given in Appendix A.2.

Lemma 3. *If conditions C_1 to C_3 are satisfied and S^{SP} is stable under the EIC-based control design, S^{SP} is stable under the PEIC-based control $\hat{\mathbf{u}}^{\text{int}}$.*

4.3 NEIC-Based Control Design

Besides the PEIC-based control, we propose an alternative controller in which the control input for \mathbf{p}_{am} is explicitly designed. We note that $\mathbf{p}_{am} \in \text{span}(\mathbf{V}_m)$ and $\mathbf{p}_{an} \in \ker(\bar{\mathbf{D}}_{ua}) = \text{span}(\mathbf{V}_n)$. The subspace $\text{span}(\mathbf{V}_m)$ and $\text{span}(\mathbf{V}_n)$ are orthogonal in \mathbb{R}^n and the motion of \mathbf{p}_{an} is independent of \mathbf{p}_{am} . Therefore, a compensation is designed in $\text{span}(\mathbf{V}_n)$ for \mathbf{p}_{an} , which leaves the motion in $\text{span}(\mathbf{V}_m)$ unchanged. Based on this observation, the NEIC-based control is designed as follows.

The NEIC-based control takes the form

$$\ddot{\mathbf{u}}^{\text{int}} = \bar{\mathbf{D}}_{aa}\ddot{\mathbf{v}}_a^{\text{int}} + \bar{\mathbf{D}}_{au}\ddot{\mathbf{q}}_u + \mathbf{H}_a^{SP}, \quad (23)$$

where $\ddot{\mathbf{v}}_a^{\text{int}} = \ddot{\mathbf{v}}_a^{\text{int}} + \ddot{\mathbf{v}}_{an}$, $\ddot{\mathbf{v}}_{an} = \mathbf{V}_n\mathbf{v}_n$, $\ddot{\mathbf{v}}_a^{\text{int}} = -\bar{\mathbf{D}}_{ua}^+(\mathbf{H}_u^{SP} + \bar{\mathbf{D}}_{uu}\ddot{\mathbf{v}}_u^{\text{int}})$, and \mathbf{v}_n is the control design that drives p_{ai} to p_{ai}^d , $i = m+1, \dots, n$. $\mathbf{p}_a^d = \mathbf{Y}(\mathbf{q}_a^d)$ is transformed reference trajectory. The design of \mathbf{v}_n compensates for the loss of original control effect $\ddot{\mathbf{v}}^{\text{ext}}$ to drive $\mathbf{e}_a \rightarrow \mathbf{0}$ in $\ker(\bar{\mathbf{D}}_{ua})$. A straightforward yet effective design of \mathbf{v}_n can be $\mathbf{v}_n = \alpha\ddot{\mathbf{v}}_n^{\text{ext}}$, where $\alpha > 0$. Compared to the PEIC-based control, \mathbf{p}_{an} plays the similar role of \mathbf{q}_{aa} coordinates. In the new coordinate, the \mathbf{q}_u is associated with \mathbf{p}_{am} only.

The following result gives the property of the NEIC-based control and the proof is given in Appendix A.3.

Lemma 4. *For S , if S^{SP} satisfies the conditions C_1 to C_3 and S^{SP} is stable under the EIC-based control, S^{SP} under the NEIC-based control $\ddot{\mathbf{v}}_a^{\text{int}}$ is also stable. Meanwhile, S_u^{SP} is unchanged compared to that under the EIC-based control.*

The proof of Lemma 4 show that the inputs $\hat{\mathbf{u}}_a^{\text{int}}$ and $\ddot{\mathbf{u}}_a^{\text{int}}$ follow the control design guidelines. Both the PEIC- and NEIC-based controllers preserve the structured form of the EIC design. Figs. 1(b) and 1(c) illustrate the overall flowchart of the PEIC- and NEIC-based control design, respectively. To take advantages the EIC-based structure, we follow the design guideline to make sure that motion of unactuated coordinates only depends on m inputs in configuration space (PEIC-based control) or transformed space (NEIC-based control). The input $\mathbf{v}_n^{\text{ext}}$ is re-used for uncontrolled motion under the NEIC-based control. The PEIC-based control assigns the balance task to a partial group of the actuated coordinates.

5 Control Stability Analysis

5.1 Closed-Loop Dynamics Under PEIC-based Control

To investigate the closed-loop dynamics, we consider the GP prediction error and BEM estimation error. The GP prediction error in (14) is extended to Δ_{aa} , Δ_{au} and Δ_u for \mathbf{q}_{aa} , \mathbf{q}_{au} , \mathbf{q}_u dynamics, respectively. Under the PEIC-based

control, the dynamics of S becomes

$$\begin{aligned} \ddot{\mathbf{q}}_{aa} &= \hat{\mathbf{v}}_a^{\text{ext}} - (\bar{\mathbf{D}}_{aa}^a)^{-1}\Delta_{aa}, \\ \ddot{\mathbf{q}}_{au} &= -(\bar{\mathbf{D}}_{ua}^u)^{-1}(\mathbf{H}_{un} + \bar{\mathbf{D}}_{uu}\hat{\mathbf{v}}_u^{\text{int}}) - (\bar{\mathbf{D}}_{aa}^u)^{-1}\Delta_{au}, \\ \ddot{\mathbf{q}}_u &= \hat{\mathbf{v}}_u^{\text{int}} - \bar{\mathbf{D}}_{uu}^{-1}[\Delta_u - \bar{\mathbf{D}}_{ua}^u(\bar{\mathbf{D}}_{aa}^u)^{-1}\Delta_{au}]. \end{aligned}$$

The BEM obtained by (17) under input $(\ddot{\mathbf{q}}_{aa}, \hat{\mathbf{v}}_u^{\text{ext}})$ is equivalent to inverting (21c) and therefore, $\hat{\mathbf{v}}_u^{\text{ext}} = -(\bar{\mathbf{D}}_{ua}^u)^{-1}\mathbf{H}_{un}|_{\mathbf{q}_u=\hat{\mathbf{q}}_u^e, \dot{\mathbf{q}}_u=\dot{\mathbf{q}}_u^e}$. Substituting the above equation into the \mathbf{q}_{au} dynamics yields $\ddot{\mathbf{q}}_{au} = \hat{\mathbf{v}}_u^{\text{ext}} + \mathbf{O}_{au}$, where $\mathbf{O}_{au} = -(\bar{\mathbf{D}}_{ua}^u)^{-1}\bar{\mathbf{D}}_{uu}\hat{\mathbf{v}}_u^{\text{int}} - (\bar{\mathbf{D}}_{aa}^u)^{-1}\Delta_{au} + \mathbf{o}_1$ and \mathbf{o}_1 denotes the higher order terms.

Defining the total error $\mathbf{e}_q = [\mathbf{e}_a^T \mathbf{e}_u^T]^T$ and $\mathbf{e} = [\mathbf{e}_q^T \hat{\mathbf{e}}_q^T]^T$, the closed-loop error dynamics becomes

$$\dot{\mathbf{e}} = \underbrace{\begin{bmatrix} \mathbf{0} & \mathbf{I}_{n+m} \\ -\hat{\mathbf{k}}_p & -\hat{\mathbf{k}}_d \end{bmatrix}}_{\mathbf{A}} \underbrace{\begin{bmatrix} \mathbf{e}_q \\ \hat{\mathbf{e}}_q \end{bmatrix}}_{\mathbf{O}_1} + \underbrace{\begin{bmatrix} \mathbf{0} \\ \mathbf{O}_{\text{tot}} \end{bmatrix}}_{\mathbf{O}_1} = \mathbf{A}\mathbf{e} + \mathbf{O}_1 \quad (24)$$

with $\mathbf{O}_{\text{tot}} = [\mathbf{O}_a^T \mathbf{O}_u^T]^T$, $\mathbf{O}_a = [\mathbf{O}_{aa}^T \mathbf{O}_{au}^T]^T$, $\mathbf{O}_{aa} = -(\bar{\mathbf{D}}_{aa}^a)^{-1}\Delta_{aa}$, $\mathbf{O}_u = -\bar{\mathbf{D}}_{uu}^{-1}(\Delta_u - \bar{\mathbf{D}}_{ua}^u(\bar{\mathbf{D}}_{aa}^u)^{-1}\Delta_{au}) - \Delta\mathbf{v}_u^{\text{int}}$, $\hat{\mathbf{k}}_p = \text{diag}(\hat{\mathbf{k}}_{p1}, \hat{\mathbf{k}}_{p2})$, and $\hat{\mathbf{k}}_d = \text{diag}(\hat{\mathbf{k}}_{d1}, \hat{\mathbf{k}}_{d2})$.

Because of bounded $\bar{\mathbf{D}}$, there exists constants $0 < d_{a1}, d_{a2}, d_{u1}, d_{u2} < \infty$ such that $d_{a1} \leq \|\bar{\mathbf{D}}_{aa}\| \leq d_{a2}$ and $d_{u1} \leq \|\bar{\mathbf{D}}_{uu}\| \leq d_{u2}$. The perturbation terms are further bounded as

$$\begin{aligned} \|\mathbf{O}_a\| &= \left\| -\begin{bmatrix} \mathbf{0} \\ (\bar{\mathbf{D}}_{ua}^u)^{-1}\bar{\mathbf{D}}_{uu}\hat{\mathbf{v}}_u^{\text{int}} \end{bmatrix} - (\bar{\mathbf{D}}_{aa}^a)^{-1}\Delta_{aa} + \begin{bmatrix} \mathbf{0} \\ \mathbf{o}_1 \end{bmatrix} \right\| \\ &\leq \frac{d_{u2}}{\sigma_1} \|\hat{\mathbf{v}}_u^{\text{int}}\| + \frac{1}{d_{a1}} \|\Delta_{aa}\| + \|\mathbf{o}_1\|, \text{ and} \\ \|\mathbf{O}_u\| &= \left\| -\bar{\mathbf{D}}_{uu}^{-1}(\Delta_u - \bar{\mathbf{D}}_{ua}^u(\bar{\mathbf{D}}_{aa}^u)^{-1}\Delta_{au}) - \Delta\mathbf{v}_u^{\text{int}} \right\| \\ &\leq \frac{1}{d_{u1}} \|\Delta_u\| + \frac{\sigma_m}{d_{u1}d_{a1}} \|\Delta_{aa}\| + \|\Delta\mathbf{v}_u^{\text{int}}\|. \end{aligned}$$

The perturbation \mathbf{o}_1 is due to approximation and $\Delta\mathbf{v}_u^{\text{int}}$ is the control difference by the BEM calculation with the GP prediction. They are both assumed to be affine with \mathbf{e} , i.e.,

$$\|\mathbf{o}_1\| \leq c_1 \|\mathbf{e}\| + c_2, \quad \|\Delta\mathbf{v}_u^{\text{int}}\| \leq c_3 \|\mathbf{e}\| + c_4 \quad (25)$$

with $0 < c_i < \infty$, $i = 1, \dots, 4$. From (19), we have $\|\mathbf{\kappa}_a^T \Sigma_a^{\frac{1}{2}}\| \leq \sigma_a^{\max} \|\mathbf{\kappa}_a\|$ and $\|\mathbf{\kappa}_u^T \Sigma_u^{\frac{1}{2}}\| \leq \sigma_u^{\max} \|\mathbf{\kappa}_u\|$. Thus, for $0 < \eta = \eta_a \eta_u < 1$, we can show that

$$\Pr\{\|\mathbf{O}_1\| \leq d_1 + d_2 \|\mathbf{e}\| + l_{u1} \|\mathbf{\kappa}_u\| + l_{a1} \|\mathbf{\kappa}_a\|\} \geq \eta, \quad (26)$$

where $d_1 = c_2 + \left(1 + \frac{d_{u2}}{\sigma_1}\right)c_4$, $d_2 = c_1 + \frac{d_{u2}}{\sigma_1}c_3$, $l_{a1} = \frac{\sigma_a^{\max}(d_{u1} + \sigma_m)}{d_{u1}d_{a1}}$, $l_{u1} = \frac{\sigma_u^{\max}}{d_{u1}}$.

5.2 Closed-Loop Dynamics Under NEIC-based Control

Plugging the NEIC-based control into \mathcal{S}^{gp} and considering Δ , we obtain

$$\ddot{\mathbf{p}}_{am} = -\Lambda_m^{-1} \mathbf{U}^T (\mathbf{H}_u^{gp} + \bar{\mathbf{D}}_{uu} \hat{\mathbf{v}}_u^{\text{int}}) - \Lambda_m^{-1} \mathbf{U}^T \Delta_u - \mathbf{V}_m^T \bar{\mathbf{D}}_{aa}^{-1} \Delta_a, \quad (27a)$$

$$\ddot{\mathbf{p}}_{an} = \mathbf{v}_n^{\text{ext}} - \mathbf{V}_n^T \bar{\mathbf{D}}_{aa}^{-1} \Delta_a, \quad (27b)$$

$$\ddot{\mathbf{q}}_u = \hat{\mathbf{v}}_u^{\text{int}} - \bar{\mathbf{D}}_{uu}^{-1} (\Delta_u - \bar{\mathbf{D}}_{ua} \bar{\mathbf{D}}_{aa}^{-1} \Delta_a). \quad (27c)$$

To obtain the error dynamics, we take advantage of the definition of BEM and from (36), we have $\mathbf{v}_a^{\text{ext}} = -\Lambda_m^{-1} \mathbf{U}^T \mathbf{H}_u^{gp} \big|_{\mathbf{q}_u = \hat{\mathbf{q}}_u^e, \dot{\mathbf{q}}_u = \ddot{\mathbf{q}}_u = \mathbf{0}}$. Then we rewrite (27a) into

$$\begin{aligned} \ddot{\mathbf{p}}_{am} = & -\Lambda_m^{-1} \mathbf{U}^T \mathbf{H}_u^{gp} \big|_{\substack{\mathbf{q}_u = \hat{\mathbf{q}}_u^e \\ \dot{\mathbf{q}}_u = \ddot{\mathbf{q}}_u = \mathbf{0}}} + \mathbf{o}_2 - \Lambda_m^{-1} \mathbf{U}^T \bar{\mathbf{D}}_{uu} \hat{\mathbf{v}}_u^{\text{int}} \\ & - \Lambda_m^{-1} \mathbf{U}^T \Delta_u - \mathbf{V}_m^T \bar{\mathbf{D}}_{aa}^{-1} \Delta_a = \mathbf{v}_m^{\text{ext}} + \mathbf{O}_m, \end{aligned} \quad (28)$$

where \mathbf{o}_2 is the residual that contains higher order terms. $\mathbf{O}_{am} = \mathbf{o}_2 - \Lambda_m^{-1} \mathbf{U}^T \bar{\mathbf{D}}_{uu} \hat{\mathbf{v}}_u^{\text{int}} - \Lambda_m^{-1} \mathbf{U}^T \Delta_u - \mathbf{V}_m^T \bar{\mathbf{D}}_{aa}^{-1} \Delta_a$ denotes the total perturbations.

The \mathcal{S}_u^{gp} dynamics keeps the same form as that in the PEIC-based control. We write the error dynamics under the NEIC-based control as

$$\ddot{\mathbf{e}}_{am} = -\hat{\mathbf{k}}_{p1} \mathbf{e}_{am} - \hat{\mathbf{k}}_{d1} \dot{\mathbf{e}}_{am} + \mathbf{O}_{am}, \quad (29a)$$

$$\ddot{\mathbf{e}}_{an} = -\hat{\mathbf{k}}_{p1} \mathbf{e}_{an} - \hat{\mathbf{k}}_{d1} \dot{\mathbf{e}}_{an} + \mathbf{O}_{an}, \quad (29b)$$

$$\ddot{\mathbf{e}}_u = -\hat{\mathbf{k}}_{p2} \mathbf{e}_u - \hat{\mathbf{k}}_{d2} \dot{\mathbf{e}}_u + \mathbf{O}_u, \quad (29c)$$

where $\mathbf{e}_{am} = \mathbf{p}_{am} - \mathbf{p}_{am}^d$, $\mathbf{e}_{an} = \mathbf{p}_{an} - \mathbf{p}_{an}^d$, $\mathbf{p}_a^d = \mathbf{V}^T \mathbf{q}_a^d$ is the image of \mathbf{q}_a^d under \mathbf{Y} , and $\mathbf{O}_{am} = -\mathbf{V}_m^T \bar{\mathbf{D}}_{aa}^{-1} \Delta_a$. Applying inverse mapping \mathbf{Y}^{-1} to (29a) and (29b), the error dynamics in \mathbf{q} is obtained as

$$\mathcal{S}_{e, \text{NEIC}} : \dot{\mathbf{e}} = \mathbf{A} \mathbf{e} + \mathbf{O}_2, \quad (30)$$

where \mathbf{O}_2 is the transformed perturbations of $[\mathbf{O}_{an}^T \mathbf{O}_{am}^T \mathbf{O}_u^T]^T$. Following the same steps in the above analysis of PEIC-based control, we obtain

$$\Pr \{ \|\mathbf{O}_2\| \leq d_1 + d_2 \|\mathbf{e}\| + l_{u2} \|\mathbf{k}_u\| + l_{a2} \|\mathbf{k}_a\| \} \geq \eta, \quad (31)$$

where $l_{u2} = \sigma_{u, \max} \frac{\sigma_1 + d_{u1}}{\sigma_1 d_{u1}}$, and $l_{a2} = \sigma_{a, \max} \frac{\sigma_m + d_{a1}}{d_{a1} d_{u1}}$. The assumption in (25) is also used for \mathbf{o}_2 .

5.3 Stability Results

To show the stability, we consider the Lyapunov function candidate $V = \mathbf{e}^T \mathbf{P} \mathbf{e} \geq 0$, where positive definite matrix $\mathbf{P} = \mathbf{P}^T$ is the solution of

$$\mathbf{A}_0^T \mathbf{P} + \mathbf{P} \mathbf{A}_0 + \mathbf{Q} = \mathbf{0}, \quad \mathbf{A}_0 = \begin{bmatrix} \mathbf{0} & \mathbf{I}_{n+m} \\ -\mathbf{k}_p & -\mathbf{k}_d \end{bmatrix} \quad (32)$$

for given positive definite matrix $\mathbf{Q} = \mathbf{Q}^T$, where \mathbf{A}_0 is the constant part of \mathbf{A} in (24) and does not depend on variances Σ_a or Σ_u . $\mathbf{k}_p = \text{diag}(\mathbf{k}_{p1}, \mathbf{k}_{p2})$ and $\mathbf{k}_d = \text{diag}(\mathbf{k}_{d1}, \mathbf{k}_{d2})$.

We denote the corresponding Lyapunov function candidates for the NEIC- and PEIC-based controls as V_1 and V_2 , respectively. The stability results are summarized as follows with the proof is given in Appendix A.4.

Theorem 1. *For robot dynamics (2), using the GP-based model (13) that satisfies conditions C_1 - C_3 , under the PEIC- and NEIC-based control, the Lyapunov function under each controller satisfies*

$$\Pr \{ \dot{V}_i \leq -\gamma_i V_i + \rho_i + \bar{\mathbf{w}}_i \} \geq \eta, \quad i = 1, 2, \quad (33)$$

and the error \mathbf{e} converges to a small ball around the origin, where γ_i is the convergence rate, ρ_i and $\bar{\mathbf{w}}_i$ are the perturbation terms, and $0 < \eta = \eta_a \eta_u < 1$.

6 Experimental Results

Two inverted pendulum platforms are used to conduct experiments to validate the control design. The results from each platform demonstrate different aspects of the control performance.

6.1 2-DOF Rotary Inverted Pendulum

Fig. 2(a) shows a 2-DOF rotary inverted pendulum that was fabricated by Quanser Inc. The base joint (θ_1) is actuated by a DC motor and the inverted pendulum joint (θ_2) is unactuated, and therefore $n = m = 1$. We use this platform to illustrate the EIC-based control and also compare the performance under different models and controllers. The robot physical model is given in [27] and can be found in Appendix B.1.

Because $m = n = 1$ and the unactuated coordinate depends on the control input, there is no uncontrolled motion when the EIC-based control is applied. Therefore, either a constant or time-varying nominal model would work for the GP-based learning control. We created the following two nominal models

$$\mathcal{S}^{n1} : \bar{\mathbf{D}}_1 = \frac{1}{100} \begin{bmatrix} 5 & -2c_2 \\ -2c_2 & 2 \end{bmatrix}, \quad \bar{\mathbf{H}}_1 = \begin{bmatrix} 0 \\ -s_2 \end{bmatrix},$$

$$\mathcal{S}^{n2} : \bar{\mathbf{D}}_2 = \frac{1}{100} \begin{bmatrix} 2 & 1 \\ 1 & 2 \end{bmatrix}, \quad \bar{\mathbf{H}}_2 = \mathbf{0},$$

where $c_i = \cos \theta_i$, $s_i = \sin \theta_i$ for angle θ_i , $i = 1, 2$. The training data were sampled and obtained from the robot system by applying control input $u = \mathbf{k}^T [\theta_1 - \theta_1' \quad \theta_2 - \theta_2' \quad \dot{\theta}_1 - \dot{\theta}_1' \quad \dot{\theta}_2 - \dot{\theta}_2']^T$, where $\mathbf{k} \in \mathbb{R}^{1 \times 4}$ and θ_i' was the combination of sine waves with different amplitudes and frequencies. We chose this input to excite the system and the gain \mathbf{k} was selected without the need to balance the platform.

We trained the GP regression models using a total of 500 data points that were randomly selected from a large

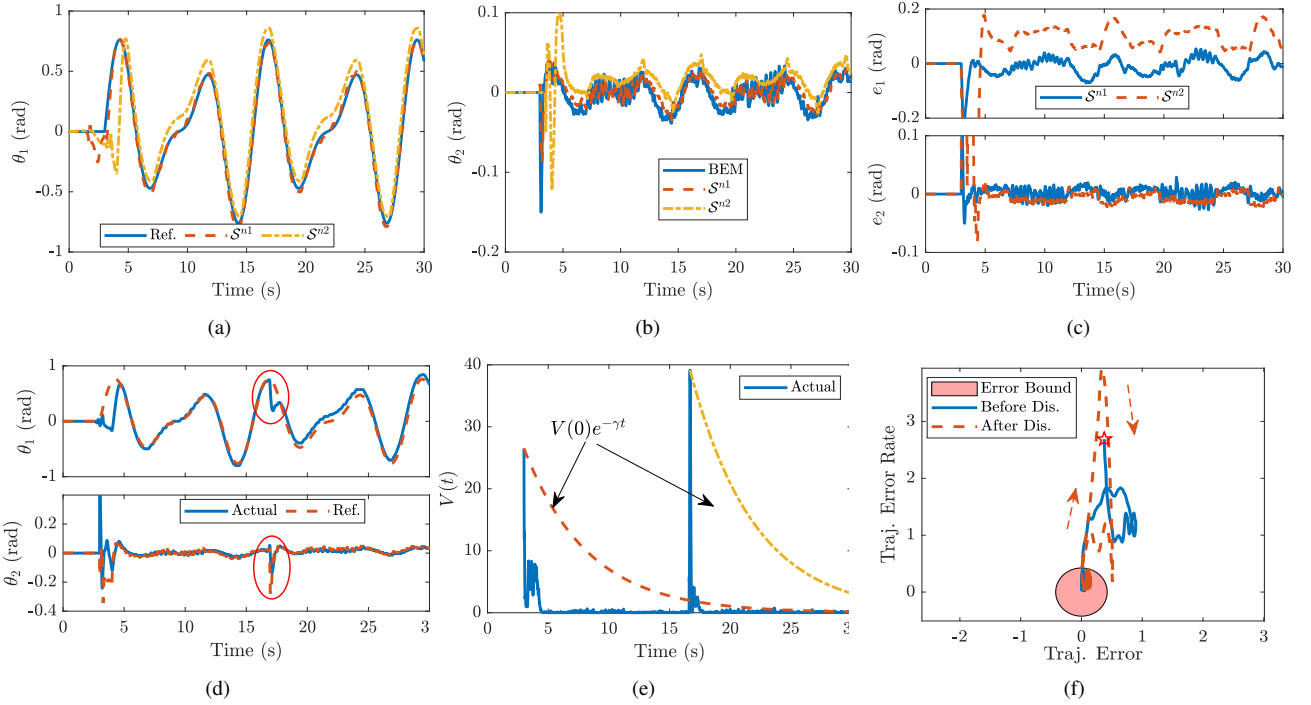


Fig. 3. Experiment results with guaranteed performance. (a) Arm rotation angle, (b) pendulum rotation angle, and (c) tracking control error under GP-based control. (d) Pendulum motion profile. (e) Profile of Lyapunov function. (f) Trajectory error motion. At $t = 17$ s, an impact disturbance is applied. The dashed arrow in (f) indicates the direction in which the error grows after disturbance is applied.

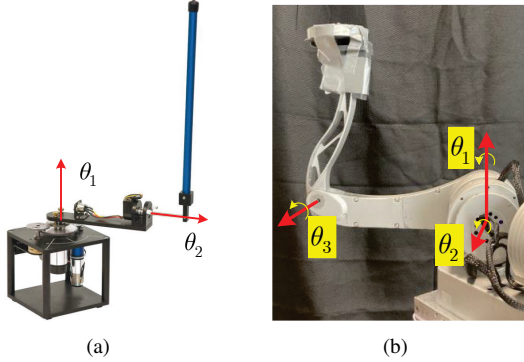


Fig. 2. (a) A Furuta pendulum. The base link joint θ_1 is actuated and the pendulum link joint θ_2 is unactuated. (b) A 3-link inverted pendulum with actuated joints θ_1 and θ_2 and unactuated joint θ_3 .

dataset. We designed the control gains as $\hat{k}_{p1} = 10 + 50\Sigma_a$, $\hat{k}_{d1} = 3 + 10\Sigma_a$, $\hat{k}_{p2} = 1000 + 500\Sigma_u$, and $\hat{k}_{d2} = 100 + 200\Sigma_u$. The variances Σ_a and Σ_u were updated online with new measurements in real time. The reference trajectory was $\theta_1^d = 0.5 \sin t + 0.3 \sin 1.5t$ rad. The control was implemented at 400 Hz in Matlab/Simulink real-time system.

Figs. 3(a) and 3(b) show the tracking of θ_1 and balance of θ_2 under the EIC-based control. With either S^{n1} or S^{n2} , the base link joint θ_1 closely followed the reference trajectory θ_1^d and the pendulum link joint θ_2 was stabilized around its equilibrium θ_2^e as well. The tracking error was reduced further and the pendulum closely followed the small variation under S^{n1} . With S^{n2} , the tracking errors became large when the base link changed rotation direction; see Fig. 3(c) at $t = 10, 17, 22$ s. Both the time-varying and constant nomi-

nal models worked for the EIC-based learning control.

Table 1 further lists the tracking errors (mean and one standard deviation) under the both GP models. For comparison purposes, we also conducted additional experiments to implement the physical model-based EIC control and the GP-based MPC design in [4]. The tracking and balance errors under the EIC-based learning control with model S^{n1} are the smallest. In particular, with the time-varying model S^{n1} , the mean values of tracking errors e_1 and e_2 were reduced by 75% and 65% respectively in comparison with those under the physical model-based EIC control. Compared with the MPC method in [4], the tracking errors with nominal model S^{n2} are at the same level.

Table 1. Tracking errors comparison under various controllers ($\times 10^{-1}$ rad)

	S^{n1}	S^{n2}	GP-based MPC [4]	Physical EIC
$ e_1 $	0.24 ± 0.17	0.96 ± 0.34	0.87 ± 0.52	1.09 ± 0.40
$ e_2 $	0.09 ± 0.05	0.09 ± 0.39	0.07 ± 0.06	0.26 ± 0.15

Fig. 3(d) shows that the control performance with nominal model S^{n1} under disturbance. At $t = 17$ s, an impact disturbance (by manually pushing the pendulum link) was applied and the joint angles changed rapidly with $\Delta\theta_1 = 0.7$ rad and $\Delta\theta_2 = 0.3$ rad. The control gains increased ($\hat{k}_{p2} = 1215$, $\hat{k}_{d2} = 143$) to respond to the disturbance. As a result, the pendulum motion tracked the BEM closely and maintained the pendulum balance after the impact disturbance. Fig. 3(e) shows the calculated Lyapunov function candidate $V(t)$ and

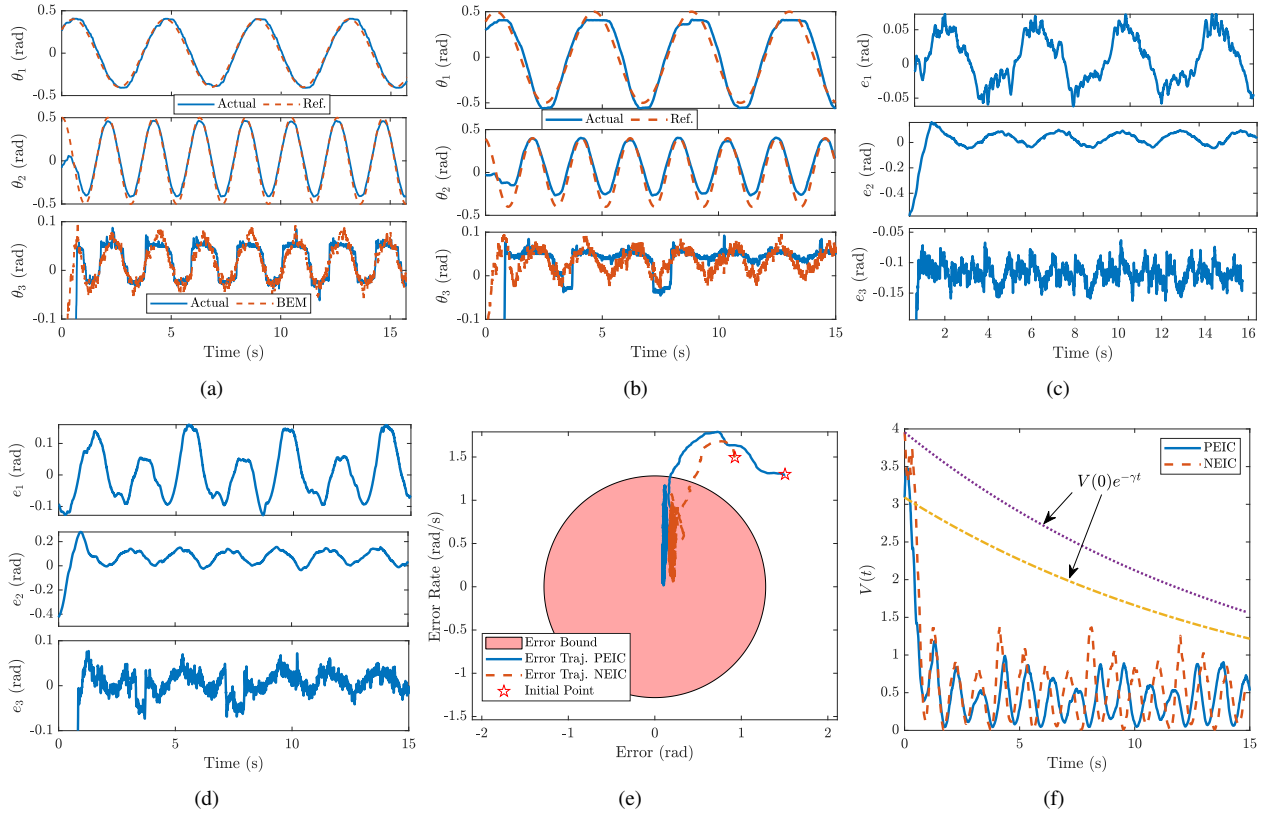


Fig. 4. Experiment results with the 3-DOF inverted pendulum. (a) and (b) Motion profiles under the PEIC- and NEIC-based control. (c) and (d) Tracking errors under the PEIC- and NEIC-based control. (e) Error trajectory in the $\|e_q\|$ - $\|e_q\|$ plane. (f) Comparison of the estimated Lyapunov function profile with the actual one.

its envelope (i.e., $V(t) = V(0)e^{-\gamma t}$, $\gamma = 0.1898$) during the experiment. Fig. 3(f) shows the error trajectory in the $\|e_q\|$ - $\|e_q\|$ plane. The solid/dashed line shows the error trajectory before/after impact disturbance. The tracking error converged quickly into the error bound. After the disturbance was applied at $t = 17$ s, both the Lyapunov function and errors grew dramatically. As the control gains increased, the errors quickly converged back to the estimated bound again.

6.2 3-DOF Rotary Inverted Pendulum

Fig. 2(b) for a 3-DOF inverted pendulum with two actuated joints (θ_1 and θ_2) and one unactuated joint (θ_3), namely, $n = 2, m = 1$. The physical model of the robot dynamics was obtained using the Lagrangian method and is given in Appendix B.2. All controllers were implemented at an updating frequency of 200 Hz through the Robot Operating System (ROS). Given the results in the previous example, the time-varying nominal model was selected as

$$\bar{D} = \begin{bmatrix} 0.15 & 0.025c_2 & 0.025c_3 \\ 0.025c_2 & 0.15 & 0.05c_{2-3} \\ 0.025c_3 & 0.05c_{2-3} & 0.1 \end{bmatrix}, \quad \bar{H} = \begin{bmatrix} 0 \\ 0.2c_2 \\ 0.1s_3 \end{bmatrix},$$

where $c_{i\pm j} = \cos(\theta_i \pm \theta_j)$. We applied an open-loop control (combination of sine wave torque) to excite the system and obtain the training dataset for the three GP models (i.e., one for each joint). The control gains were $\hat{k}_{p1} =$

$15I_2 + 20\Sigma_a, \hat{k}_{d1} = 3I_2 + 10\Sigma_a, \hat{k}_{p2} = 25 + 20\Sigma_u, \hat{k}_{d2} = 5.5 + 10\Sigma_u$, where GP variances Σ_a and Σ_u were updated on-line in real time. The reference trajectory was chosen as $\theta_1^d = 0.5 \sin 1.5t$, $\theta_2^d = 0.4 \sin 3t$ rad.

For the PEIC-based control, we chose $q_{aa} = \theta_1$ and $q_{au} = \theta_2$ and the NEIC-based control was $\mathbf{v}_n = \hat{\mathbf{v}}_n^{\text{ext}}$. Fig. 4 shows the experimental results under the PEIC- and NEIC-based control. Under both controllers, the actuated joints (θ_1 and θ_2) followed the given reference trajectories (θ_1^d and θ_2^d) closely and the unactuated joint (θ_3) was balanced around the BEM (θ_3^e) as shown in Figs. 4(a) and 4(b). The pendulum link motion displayed a similar pattern for both controllers. However, the tracking error e_1 under the PEIC-based control (i.e., from -0.05 to 0.05 rad) was much smaller than that under the NEIC-based control (i.e., from -0.15 to 0.15 rad); see Figs. 4(c) and 4(d). The balance task in the PEIC-based control was assigned to joint θ_2 and joint θ_1 is viewed as virtually independent of θ_2 and θ_3 . Joint θ_1 achieved almost-perfect tracking control regardless of the errors for θ_2 and θ_3 . The compensation effect in the null space appeared in the entire configuration space and any motion error in the unactuated joints affected the motion of all actuated joints. Similar to the previous example, Fig. 4(e) shows the error trajectory profile in the $\|e_q\|$ - $\|e_q\|$ plane. Fig. 4(f) shows the Lyapunov function profiles under the PEIC- and NEIC-based controls.

Fig. 5 shows the motion of the actuated coordinate in the transformed coordinate \mathbf{p}_a under various controllers. Un-

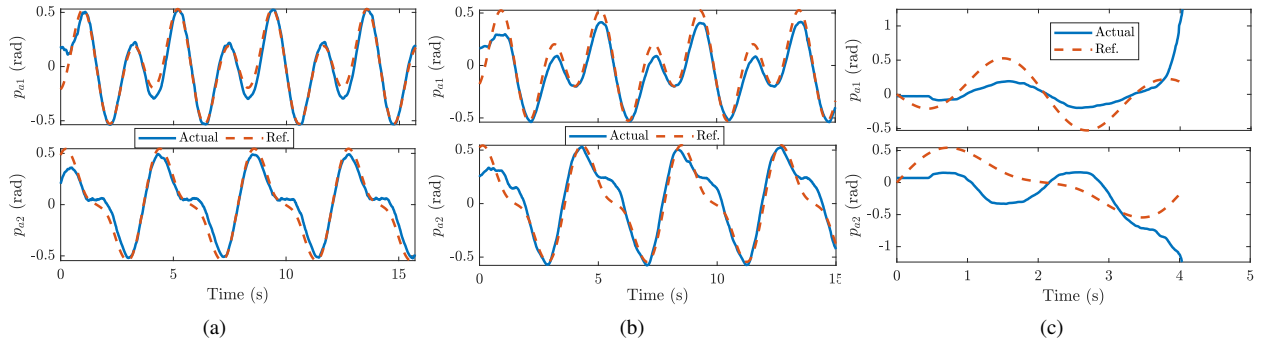


Fig. 5. Motion profiles of robotic leg in transformed space under (a) PEIC-based control, (b) NEIC-based control, and (c) EIC-based control.

Table 2. Statistical Analysis of Tracking Performance (Mean and Standard Deviation for Errors) Under Different Controllers

	$ e_1 $ (rad)	$ e_2 $ (rad)	$ e_3 $ (rad)	$\ e\ $	$\int \mathbf{u}^T \mathbf{u} dt$
PEIC (GP)	0.0302 ± 0.0178	0.0566 ± 0.0685	0.1182 ± 0.0160	0.1343 ± 0.0166	5.7659
NEIC (GP, $\alpha = 0.5$)	0.1395 ± 0.0946	0.1166 ± 0.0512	0.0303 ± 0.0209	0.2001 ± 0.0770	5.9022
NEIC (GP, $\alpha = 1.0$)	0.0651 ± 0.0416	0.0756 ± 0.0481	0.0195 ± 0.0152	0.1101 ± 0.0499	5.7089
NEIC (GP, $\alpha = 1.5$)	0.0376 ± 0.0302	0.0792 ± 0.0482	0.0207 ± 0.0169	0.0972 ± 0.0470	5.7305
PEIC (Model)	0.2168 ± 0.1165	0.2398 ± 0.1649	0.0179 ± 0.0140	0.3587 ± 0.1307	5.7978
NEIC (Model, $\alpha = 1.0$)	0.1374 ± 0.0922	0.1237 ± 0.0597	0.0455 ± 0.0385	0.2095 ± 0.0769	5.8452

der the PEIC- and NEIC-based controls, the \mathbf{p}_a variables followed the reference profile \mathbf{p}_a^d as shown in Figs. 5(a) and 5(b). Fig. 5(c) shows the motion profile under the EIC-based control. In the first 2 seconds, joint θ_3 followed the BEM under the EIC-based control and p_{a1} coordinates displayed a similar motion pattern. However, p_{a2} coordinate showed diverge behavior and led to fall completely. Therefore, as analyzed previously, the system became unstable under the EIC-based control though conditions \mathcal{C}_1 to \mathcal{C}_3 were satisfied.

For the fixed NEIC-based control \mathbf{v}^{int} for balancing the unactuated subsystem, we can reduce the tracking error by updating \mathbf{v}_n with increased α values. Fig. 6 shows the experiment results of the \mathbf{p}_a error profiles under various α values varying from 0.5 to 1.5. With a large α value, the tracking error of actuated coordinates was reduced. Table 2 further lists the steady-state errors (in joint angles) under the NEIC-based control with various α values, the PEIC-based control and the physical model-based control design. Under the NEIC-based control with $\alpha = 0.5$, the system was stabilized; when increasing α values to 1 and 1.5, the mean tracking errors were reduced 50% and 70% for θ_1 , respectively, and 40% for θ_2 . Since control input \mathbf{v}_n did not affect the balance task of the unactuated subsystem, the tracking errors for θ_3 maintained at the same level. It is of interest that the control effort (i.e., last column in Table 2) only shows a slight increase with large α values.

6.3 Discussion

For the rotary pendulum example, we have $n = m$ and the null space $\ker(\mathbf{D}_{au})$ vanishes. The compensation effect is no longer needed by the NEIC-based control, i.e., $\tilde{\mathbf{v}}_a^{\text{int}} = \tilde{\mathbf{v}}^{\text{int}}$

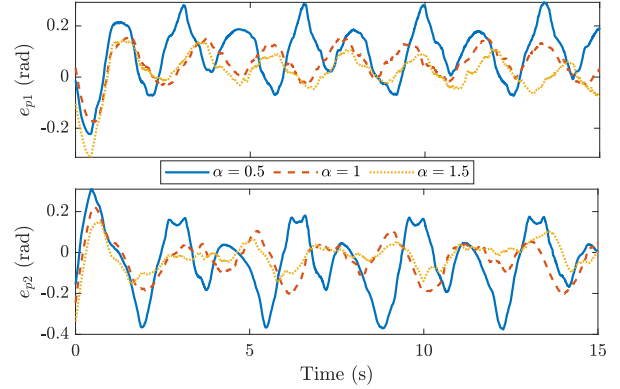


Fig. 6. The tracking errors in coordinate \mathbf{p}_a under the NEIC-based control with various α values.

and $\tilde{\mathbf{u}}^{\text{int}} = \bar{\mathbf{D}}_{aa}\tilde{\mathbf{v}}_a^{\text{int}} + \bar{\mathbf{D}}_{au}\tilde{\mathbf{q}}_u + \mathbf{H}_a^{gp} = \mathbf{u}^{\text{int}}$. In this case, the PEIC- and NEIC-based controls are degenerated to the EIC-based control. For the 3-DOF inverted pendulum, the control inputs u_1 and u_2 act on θ_3 joints through $\ddot{\theta}_1$ and $\ddot{\theta}_2$. Therefore, as shown in Lemma 1, the uncontrolled motion exists since all controls show up in S_u dynamics. This observation explains why the EIC-based control failed to balance the three-link inverted pendulum. If the S_u dynamics is related to m control inputs (through $\tilde{\mathbf{q}}_a$) for $n > m$ such as the bikebot dynamics in [4, 25], only m external controls were updated and the EIC-based control worked well without any uncontrolled motion.

For the PEIC-based control, the robot dynamics were partitioned into $\mathcal{S}^{gp} = \{\mathcal{S}_{aa}^{gp}, \{\mathcal{S}_{au}^{gp}, \mathcal{S}_u^{gp}\}\}$, which contains a fully actuated system \mathcal{S}_{aa}^{gp} , and a reduced-order underactuated system $\{\mathcal{S}_{au}^{gp}, \mathcal{S}_u^{gp}\}$. The EIC-based control is applied

to \mathcal{S}_{au}^{gp} and \mathcal{S}_u^{gp} only. The dynamics of \mathbf{q}_u in general does not depend on any specific m actuated coordinates, since the mapping \mathbf{Y} is time-varying across different control cycles. In the NEIC-based control design, \mathbf{p}_{am} and \mathbf{q}_u become an underactuated subsystem and \mathbf{p}_{an} is fully actuated.

In practice, no specific rules are specified to select \mathbf{q}_{au} out of \mathbf{q}_a coordinates, and therefore, there are a total of $C_n^m = \frac{n!}{m!(n-m)!}$ options to select different coordinates. We can take advantage of such a property to optimize tracking performance for selected coordinates. In the 3-DOF pendulum case, we assigned the balance task of θ_3 to θ_2 motion. The length of link 1 was only 0.09 m, which was much shorter than the length of link 2 (0.23 m). The coupling effect between θ_2 and θ_3 was much stronger than that between θ_1 and θ_3 ; see D_{13} and D_{23} in Appendix B.2. Thus, it was efficient to use the motion of θ_2 as a virtual control input to balance θ_3 . When implementing the PEIC-based controller with $q_{au} = \theta_1$, the system cannot achieve the desired performance and becomes unstable. We also implemented the proposed controller with the physical model. The control errors are included and listed in Table 2. Compared with the learning-based controllers, the model-based control resulted in larger errors. Since the mechanical frictions and other unstructured effects were not considered, the physical model might not capture and reflect the accurate robot dynamics. The results confirmed the advantages of the proposed learning-based control approaches.

7 Conclusion

This paper presented a new learning-based modeling and control framework for underactuated balance robots. The proposed design was an extension and improvement of the EIC-based control with a GP-enabled robot dynamics. The proposed new robot controllers preserved the structural design of the EIC-based control and achieved both tracking and balance tasks. The PEIC-based control re-shaped the coupling between the actuated and unactuated coordinates. The robot dynamics was transferred into a fully actuated subsystem and one reduced-order underactuated balance system. The NEIC-based control compensated for uncontrolled motion in a subspace. We validated and demonstrated the new control design on two experimental platforms and confirmed that stability and balance were guaranteed. The comparison with the physical model-based EIC control and the MPC design confirmed superior performance in terms of the error bound. Extension of the GP-based learning control design for highly underactuated balance robots is one of the ongoing research directions.

Acknowledgments

The work was supported in part by the US National Science Foundation (NSF) under award CNS-1932370.

Appendices

A Proofs

A.1 Proof of Lemma 1

The system dynamics \mathcal{S} under the control \mathbf{u}^{ext} is

$$\ddot{\mathbf{q}}_a = \mathbf{v}^{\text{ext}}, \quad \ddot{\mathbf{q}}_u = -\mathbf{D}_{uu}^{-1}(\mathbf{D}_{ua}\mathbf{v}^{\text{ext}} + \mathbf{H}_u). \quad (34)$$

When $\text{rank}(\mathbf{D}_{au}) = m$ holds for \mathbf{q} , the SVD in (7) exists and all m singular values are great than zero, i.e., $\sigma_i > 0$. Thus $\ker(\mathbf{D}_{au}) = \mathbf{V}_n$ contains $(n - m)$ column vectors. Plugging (7) into (34) and considering the coordinate transformation, we obtain

$$\ddot{\mathbf{p}}_a = \mathbf{v}^{\text{ext}}, \quad \ddot{\mathbf{q}}_u = -\mathbf{D}_{uu}^{-1}(\mathbf{U}\mathbf{\Lambda}_m\mathbf{v}_m^{\text{ext}} + \mathbf{H}_u), \quad (35)$$

where $\mathbf{U}\mathbf{\Lambda}\mathbf{V}^T\mathbf{v}^{\text{ext}} = \mathbf{U}\mathbf{\Lambda}_m\mathbf{v}_m^{\text{ext}}$ is obtained and used by using the fact that $\mathbf{\Lambda} \in \mathbb{R}^{m \times n}$ is a rectangular diagonal matrix.

Given the definition of \mathcal{E} , \mathbf{q}_u^e is obtained by solving the algebraic equation $\mathbf{\Gamma}_0(\mathbf{q}_u; \mathbf{v}^{\text{ext}}) = \mathbf{0}$. We replace $\mathbf{D}_{ua}(\mathbf{q}_u^e)$ with $\mathbf{D}_{ua}(\mathbf{q}_u)$ in $\mathbf{\Gamma}_0$ and therefore, using (7), $\mathbf{\Gamma}_0 = \mathbf{0}$ is rewritten into

$$\mathbf{\Lambda}_m\mathbf{v}_m^{\text{ext}} + \mathbf{U}^T\mathbf{H}_u^{gp} \Big|_{\mathbf{q}_u=\mathbf{q}_u^e, \dot{\mathbf{q}}_u=\dot{\mathbf{q}}_u^e} = \mathbf{0}. \quad (36)$$

The BEM \mathcal{E} depends only on $\mathbf{v}_m^{\text{ext}}$. That is, the control effect in $\ker(\mathbf{D}_{ua})$ is not used when obtaining the BEM.

Furthermore, since all controls show up in \mathcal{S}_u dynamics, the control inputs should be updated and the EIC-based control in (6) exists. We substitute (7) and (6) into \mathcal{S}_a dynamics and obtain

$$\ddot{\mathbf{q}}_a = \mathbf{v}^{\text{int}} = -\mathbf{D}_{ua}^+(\mathbf{H}_u + \mathbf{D}_{uu}\mathbf{v}_u^{\text{int}}) = -\mathbf{V}\mathbf{\Lambda}^+\mathbf{U}^T(\mathbf{H}_u + \bar{\mathbf{D}}_u\mathbf{v}_u^{\text{int}}).$$

Multiplying the above equation on both sides with \mathbf{V}^T and considering (8), \mathcal{S} under the EIC-based control becomes (9) and the $(n - m)$ coordinates are free of control.

A.2 Proof of Lemma 3

Under input \mathbf{u}_u , $\ddot{\mathbf{q}}_{au} = \mathbf{v}_{au}^{\text{int}}$, we solve $\ddot{\mathbf{q}}_u$ by (21c),

$$\begin{aligned} \ddot{\mathbf{q}}_u &= -\bar{\mathbf{D}}_{uu}^{-1}[\bar{\mathbf{D}}_{ua}^u\mathbf{v}_{au}^{\text{int}} + \mathbf{H}_{un}] \\ &= -\bar{\mathbf{D}}_{uu}^{-1}[\mathbf{H}_{un} - \bar{\mathbf{D}}_{ua}^u(\bar{\mathbf{D}}_{ua}^u)^{-1}(\mathbf{H}_{un} + \bar{\mathbf{D}}_{uu}\hat{\mathbf{v}}_u^{\text{int}})] = \hat{\mathbf{v}}_u^{\text{int}}. \end{aligned}$$

Clearly, the unperturbed subsystem \mathcal{S}_u^{gp} remains the same as that under the EIC-based control. With the designed control, the \mathbf{q}_{aa} dynamics is unchanged and $\ddot{\mathbf{q}}_{aa} = \hat{\mathbf{v}}_a^{\text{ext}}$ holds regardless of $\hat{\mathbf{v}}_u^{\text{int}}$. For \mathbf{q}_{aa} and \mathbf{q}_{au} , we obtain $\ddot{\mathbf{q}}_{aa} = \hat{\mathbf{v}}_a^{\text{ext}}$ and $\ddot{\mathbf{q}}_{au} = \hat{\mathbf{v}}_u^{\text{int}}$. The relationship in (9) indicates that if the unactuated subsystem dynamics is written into $\ddot{\mathbf{q}}_u = \mathbf{v}_u^{\text{int}}$, the dynamics $\ddot{\mathbf{q}}_a$ under the transformation \mathbf{Y} must contain the

portion (9a). Similarly, we obtain

$$S_{\text{PEIC}} : \ddot{p}_{ai} = -\frac{\mathbf{u}_i^T (\mathbf{H}_u^{gp} + \bar{\mathbf{D}}_{uu} \hat{\mathbf{v}}_u^{\text{int}})}{\sigma_i}, \quad i = 1, \dots, m, \quad (37a)$$

$$\ddot{p}_{aj} = \mathbf{v}_j^T \hat{\mathbf{v}}_a^{\text{int}}, \quad j = m+1, \dots, n, \quad (37b)$$

$$\ddot{\mathbf{q}}_u = \hat{\mathbf{v}}_u^{\text{int}}, \quad (37c)$$

where $\hat{\mathbf{v}}_a^{\text{int}} = [(\hat{\mathbf{v}}_a^{\text{ext}})^T (\hat{\mathbf{v}}_u^{\text{int}})^T]^T$. Since $\hat{\mathbf{v}}_a^{\text{int}}$ is not obtained in the way as in (5), i.e., $\hat{\mathbf{v}}_a^{\text{int}} \notin \ker(\bar{\mathbf{D}}_{ua})$, $\mathbf{v}_{m+j}^T \hat{\mathbf{v}}_a^{\text{int}} \neq \mathbf{0}$ and \mathbf{p}_{am} is under active control design. Meanwhile $\mathbf{v}_{m+j}^T \hat{\mathbf{v}}_a^{\text{int}}$ drives $\mathbf{q}_a \rightarrow \mathbf{q}_a^d$ in $\ker(\bar{\mathbf{D}}_{ua})$, given that $\hat{\mathbf{v}}_a^{\text{ext}}$ and $\hat{\mathbf{v}}_u^{\text{int}}$ are designed to drive $\mathbf{q}_a \rightarrow \mathbf{q}_a^d$. Therefore, if the unperturbed system under EIC-based control is stable, it is also stable under the PEIC-based control. This completes the proof.

A.3 Proof of Lemma 4

Under the NEIC-based control input, the S_a^{gp} becomes

$$\ddot{\mathbf{q}}_a = \hat{\mathbf{v}}_a^{\text{int}} = \hat{\mathbf{v}}_u^{\text{int}} + \hat{\mathbf{v}}_a^{\text{ext}} = -\bar{\mathbf{D}}_{ua}^+ (\mathbf{H}_u^{gp} + \bar{\mathbf{D}}_{uu} \hat{\mathbf{v}}_u^{\text{int}}) + \mathbf{V}_n \mathbf{v}_n. \quad (38)$$

Plugging above equation into S_u^{gp} , we obtain

$$\ddot{\mathbf{q}}_u = -\bar{\mathbf{D}}_{uu}^{-1} (\bar{\mathbf{D}}_{ua} \ddot{\mathbf{q}}_a + \mathbf{H}_u^{gp}) = -\bar{\mathbf{D}}_{uu}^{-1} [-\bar{\mathbf{D}}_{ua} \bar{\mathbf{D}}_{ua}^+ (\mathbf{H}_u^{gp} + \bar{\mathbf{D}}_{uu} \hat{\mathbf{v}}_u^{\text{int}}) + \bar{\mathbf{D}}_{ua} \mathbf{V}_n \mathbf{v}_n + \mathbf{H}_u^{gp}] = \hat{\mathbf{v}}_u^{\text{int}} - \bar{\mathbf{D}}_{uu}^{-1} \bar{\mathbf{D}}_{ua} \mathbf{V}_n \mathbf{v}_n.$$

Using the SVD form of $\bar{\mathbf{D}}_{ua}$ in (7) and $\mathbf{A} \mathbf{V}^T \mathbf{V}_n \equiv \mathbf{0}$, the above equation is further simplified as

$$\ddot{\mathbf{q}}_u = \hat{\mathbf{v}}_u^{\text{int}} - \bar{\mathbf{D}}_{uu}^{-1} \mathbf{U} \mathbf{A} \mathbf{V}^T \mathbf{V}_n \mathbf{v}_n = \hat{\mathbf{v}}_u^{\text{int}}. \quad (39)$$

Clearly, S_u^{gp} dynamics is unchanged compared to (9).

We further apply the transformation \mathbf{Y} to \mathbf{q}_a and apply SVD to $\bar{\mathbf{D}}_{ua}^+$. The S_u dynamics (38) and (39) become

$$S_{\text{NEIC}} : \ddot{p}_{ai} = -\frac{\mathbf{u}_i^T (\mathbf{H}_u^{gp} + \bar{\mathbf{D}}_{uu} \hat{\mathbf{v}}_u^{\text{int}})}{\sigma_i}, \quad i = 1, \dots, m, \quad (40a)$$

$$\ddot{p}_{aj} = \mathbf{v}_{nj}, \quad j = m+1, \dots, n, \quad (40b)$$

$$\ddot{\mathbf{q}}_u = \hat{\mathbf{v}}_u^{\text{int}}. \quad (40c)$$

Compared to (9), we add the control $\hat{\mathbf{v}}_a^{\text{ext}}$ to drive $\mathbf{q}_a \rightarrow \mathbf{q}_a^d$ in the subspace $\ker(\bar{\mathbf{D}}_{ua})$. Therefore, if the system (9) is stable, (37) is also stable, as the \mathbf{p}_{am} and \mathbf{q}_u dynamics are unchanged.

A.4 Proof for Theorem 1

We present the stability proof for the PEIC- and NEIC-based controls using the Lyapunov method.

PEIC-Based Control: Plugging (24) into the $V_1 = V$ and considering (32), we obtain $\dot{V}_1 = \mathbf{e}^T (\mathbf{A}^T \mathbf{P} + \mathbf{P} \mathbf{A}) \mathbf{e} +$

$2\mathbf{e}^T \mathbf{P} \mathbf{O}_1 = -\mathbf{e}^T \mathbf{Q} \mathbf{e} + \mathbf{e}^T \mathbf{Q}_\Sigma \mathbf{e} + 2\mathbf{e}^T \mathbf{P} \mathbf{O}_1$, where $\mathbf{Q}_\Sigma = (\mathbf{A} - \mathbf{A}_0)^T \mathbf{P} + \mathbf{P} (\mathbf{A} - \mathbf{A}_0)$. The bounded variance leads to the bounded eigenvalue of matrix \mathbf{Q}_Σ . Given the fact that $\mathbf{Q}_\Sigma = \mathbf{Q}_\Sigma^T$, the eigenvalues of \mathbf{Q}_Σ are real numbers.

We note that \mathbf{Q}_Σ is bounded and \mathbf{P}, \mathbf{Q} are constant. The perturbation term \mathbf{O}_1 is bounded as shown in (26). Then \dot{V}_1 is rewritten as

$$\begin{aligned} \dot{V}_1 &\leq -[\lambda_{\min}(\mathbf{Q}) - \lambda_{\max}(\mathbf{Q}_\Sigma)] \|\mathbf{e}\|^2 + 2\lambda_{\max}(\mathbf{P}) \|\mathbf{e}\| (d_1 \\ &\quad + d_2 \|\mathbf{e}\|) + 2\lambda_{\max}(\mathbf{P}) \|\mathbf{e}\| (l_{u1} \|\mathbf{k}_u\| + l_{a1} \|\mathbf{k}_a\|) \\ &= -[\lambda_{\min}(\mathbf{Q}) - \lambda_{\min}(\mathbf{Q}_\Sigma) - 2d_2 \lambda_{\max}(\mathbf{P})] \|\mathbf{e}\|^2 \\ &\quad + 2(d_1 + \omega_1) \lambda_{\max}(\mathbf{P}) \|\mathbf{e}\|. \end{aligned}$$

where $\omega_1 = l_{u1} \|\mathbf{k}_u\| + l_{a1} \|\mathbf{k}_a\|$ denotes the uncertainties related to GP prediction errors. $\lambda_{\min}(\cdot)$ and $\lambda_{\max}(\cdot)$ denote the smallest and greatest eigenvalues of a matrix, respectively. Considering $\lambda_{\min}(\mathbf{P}) \|\mathbf{e}\|^2 \leq V_1 \leq \lambda_{\max}(\mathbf{P}) \|\mathbf{e}\|^2$, we define

$$\gamma_1 = \frac{\lambda_{\min}(\mathbf{Q}) - \lambda_{\max}(\mathbf{Q}_\Sigma) - 2d_2 \lambda_{\max}(\mathbf{P})}{\lambda_{\max}(\mathbf{P})},$$

$\rho_1 = 2d_1 \lambda_{\max}(\mathbf{P}) \|\mathbf{e}\|$, $\varpi_1 = 2\omega_1 \lambda_{\max}(\mathbf{P}) \|\mathbf{e}\|$. With the bounded perturbations ρ_1 and ω_1 , the closed-loop system dynamics can be shown stable in the sense of probability as $\Pr\{V_1 \leq -\gamma_1 V_1 + \rho_1 + \varpi_1\} > \eta$. Taking further analysis, we obtain a nominal estimation of the error convergence performance using the Lyapunov function as $\Pr\{\dot{V}_1 \leq V_1(0)e^{-\gamma_1 t}\} > \eta$ and the error bound estimation $\Pr\{\|\mathbf{e}\| \leq r_1\} > \eta$ with $r_1 = \frac{2d_1 \lambda_{\max}(\mathbf{P})}{\lambda_{\min}(\mathbf{Q}) - \lambda_{\max}(\mathbf{Q}_\Sigma) - 2d_2 \lambda_{\max}(\mathbf{P})}$.

NEIC-Based Control: Without the loss of generality, we select $\mathbf{v}_n = \mathbf{V}_n^T \hat{\mathbf{v}}_a^{\text{ext}}$. We take $V_2 = V$ as the Lyapunov function candidate for $S_{e,\text{NEIC}}$. If the control gains are the same as that in PEIC-based control and $\alpha = 1$ for compensation effect, $\gamma_2 = \gamma_1$. We choose control gains properly such that $\gamma_2 > 0$. The system can be shown stable as $\Pr\{\dot{V}_2 \leq -\gamma_2 V_2 + \rho_2 + \varpi_2\} > \eta$, where $\rho_2 = 2d_1 \lambda_{\max}(\mathbf{P}) \|\mathbf{e}\|$, $\varpi_2 = 2\omega_2 \lambda_{\max}(\mathbf{P}) \|\mathbf{e}\|$, and $\omega_2 = l_{u2} \|\mathbf{k}_u\| + l_{a2} \|\mathbf{k}_a\|$ is defined same as ω_1 containing the GP prediction uncertainties. A nominal estimation of error convergence and final error bound can also be obtained.

To show $\gamma_i > 0$, $i = 1, 2$, the control gains should be properly selected. We assume that during the training data collection phase, the physical system is fully excited. The GP models are accurate compared to physical models. With a small predefined error limit as a stop criterion in BEM estimation, c_i values can be shown as $c_i \ll 1$. Given the explicit form, d_i are estimated for \mathbf{A}_0 and \mathbf{Q}, \mathbf{P} is obtained by solving (32). The matrix \mathbf{Q}_Σ depends on the control gains associated with the prediction variance. Since the variance is bounded, we design \mathbf{k}_{ni} such that $\lambda_{\max}(\mathbf{Q}_\Sigma)$ satisfies the inequality $\lambda_{\min}(\mathbf{Q}) - \lambda_{\max}(\mathbf{Q}_\Sigma) - 2d_2 \lambda_{\max}(\mathbf{P}) > 0$. Thus the stability is obtained.

B Dynamics Model of Underactuated Balance Robots

B.1 Rotary inverted pendulum

The dynamics model for the rotary pendulum is in the form of (1) with $q_a = \theta_1$ and $q_u = \theta_2$. The model parameters are $\mathbf{B} = [1 \ 0]^T$ and

$$\begin{aligned} D_{aa} &= C(m_p l_r^2 + 0.25 m_p l_p^2 s_2^2 + J_r), \\ D_{au} &= D_{ua} = -0.5 C m_p l_p l_r c_\alpha, \quad D_{uu} = C(J_p + 0.25 m_p l_p^2), \\ H_a &= C(0.5 m_p l_p^2 \dot{\theta}_1 \dot{\theta}_2 s_2 c_2 + 0.5 m_p l_p l_r \dot{\theta}_2^2 s_\alpha + \\ &\quad d_r \dot{\theta}_1 + k_g^2 k_t k_m \dot{\theta}_1 / R_m) + K_g k_t \dot{\theta}_2, \\ H_u &= C(d_p \dot{\theta}_2 - 0.25 m_p l_p^2 c_2 s_2 \dot{\theta}^2 - 0.5 m_p l_p g s_2), \end{aligned}$$

where l_r , J_r and d_r are the length, mass inertia and viscous damping coefficient of the base link, l_p , J_p and d_p are corresponding parameters of the pendulum, m_p is the pendulum mass, g is the gravitational constant, and k_t, k_m, K_g, R_m, C are robot constant. The values of these parameters can be found in [27]. The control input is the motor voltage, i.e., $u = V_m$.

B.2 3-link inverted pendulum

The model parameters for the 3-link inverted pendulum in (1) are

$$\begin{aligned} D_{11} &= (m_3(l_2^2 + 0.25 l_3^2) + 0.25 m_2 l_2^2 - 0.5 m_3 l_3^2 c_3^2 - m_3 l_2 l_3 s_3) c_2^2 \\ &\quad + (0.5 m_3 s_3 l_3^2 - m_3 l_2 l_3) s_2 c_3 c_2 + 0.25 m_3 c_3^2 l_3^2 \\ &\quad + (0.25 m_1 + m_2 + m_3) l_1^2 + J_1, \\ D_{12} &= D_{21} = -(m_3 l_2 + 0.5 m_2 l_2) l_1 s_2 - 0.5 m_3 l_1 l_3 c_{2+3}, \\ D_{13} &= D_{31} = 0.5 m_3 l_1 l_3 c_{2+3}, \\ D_{22} &= J_2 + (m_3 + 0.25 m_2) l_2^2 + 0.25 m_3 l_3^2 - m_3 l_2 l_3 s_3, \\ D_{23} &= D_{32} = (0.25 l_3 - 0.5 l_2 s_3) m_3 l_3, \quad D_{33} = J_3 + 0.25 m_3 l_3^2, \\ G_1 &= 0, \quad G_2 = -(0.5 m_2 + m_3) c_2 l_2 g + 0.5 m_3 l_3 s_{2+3} g, \\ G_3 &= -0.5 m_3 l_3 s_{2+3} g, \end{aligned}$$

where m_i , l_i and J_i are the mass, length, and mass inertia of each link, and $s_{i+j} = \sin(\theta_i + \theta_j)$. Matrix \mathbf{C} is obtained as $C_{ij} = \sum_{k=1}^3 c_{ijk} \dot{\theta}_k$, where Christoffel symbols $c_{ijk} = \frac{1}{2} \left(\frac{\partial D_{ij}}{\partial \dot{\theta}_k} + \frac{\partial D_{jk}}{\partial \dot{\theta}_i} - \frac{\partial D_{ik}}{\partial \dot{\theta}_j} \right)$. The physical parameters are $m_1 = 0.7$ kg, $m_2 = 1.3$ kg, $m_3 = 0.3$ kg, $l_1 = 0.065$ m, $l_2 = 0.23$ m, $l_3 = 0.25$ m, $J_1 = 0.0008$ kgm², $J_2 = 0.005$ kgm², $J_3 = 0.003$ kgm².

References

- [1] Kant, N., and Mukherjee, R., 2020. "Orbital stabilization of underactuated systems using virtual holonomic constraints and impulse controlled poincaré maps". *Syst. Contr. Lett.*, **146**, pp. 1–9. article 104813.
- [2] Han, F., and Yi, J., 2023. "On the learned balance manifold of underactuated balance robots". In *Proc. IEEE Int. Conf. Robot. Autom.*, pp. 12254–12260.
- [3] Han, F., Jelvani, A., Yi, J., and Liu, T., 2022. "Coordinated pose control of mobile manipulation with an unstable bikebot platform". *IEEE/ASME Trans. Mechatronics*, **27**(6), pp. 4550–4560.
- [4] Chen, K., Yi, J., and Song, D., 2023. "Gaussian-process-based control of underactuated balance robots with guaranteed performance". *IEEE Trans. Robotics*, **39**(1), pp. 572–589.
- [5] Han, F., and Yi, J., 2021. "Stable learning-based tracking control of underactuated balance robots". *IEEE Robot. Automat. Lett.*, **6**(2), pp. 1543–1550.
- [6] Turrissi, G., Capotondi, M., Gaz, C., Modugno, V., Oriolo, G., and Luca, A. D., 2022. "On-line learning for planning and control of underactuated robots with uncertain dynamics". *IEEE Robot. Automat. Lett.*, **7**(1), pp. 358–365.
- [7] Beckers, T., Kulić, D., and Hirche, S., 2019. "Stable Gaussian process based tracking control of Euler–Lagrange systems". *Automatica*, **103**, pp. 390–397.
- [8] Chen, K., and Yi, J., 2015. "On the relationship between manifold learning latent dynamics and zero dynamics for human bipedal walking". In *Proc. IEEE/RSJ Int. Conf. Intell. Robot. Syst.*, pp. 971–976.
- [9] Grizzle, J. W., Chevallereau, C., Sinnet, R. W., and Ames, A. D., 2014. "Models, feedback control, and open problems in 3D bipedal robotic walking". *Automatica*, **50**, pp. 1955–1988.
- [10] Han, F., Huang, X., Wang, Z., Yi, J., and Liu, T., 2022. "Autonomous bikebot control for crossing obstacles with assistive leg impulsive actuation". *IEEE/ASME Trans. Mechatronics*, **27**(4), pp. 1882–1890.
- [11] Shiriaev, A. S., Perram, J. W., and Canudas-de-Wit, C., 2005. "Constructive tool for orbital stabilization of underactuated nonlinear systems: Virtual constraints approach". *IEEE Trans. Automat. Contr.*, **50**(8), pp. 1164–1176.
- [12] Canudas-de-Wit, C., Espiau, B., and Urrea, C., 2002. "Orbital stabilization of underactuated mechanical systems". *IFAC Proceedings Volumes*, **35**(1), pp. 527–532. 15th IFAC World Congress.
- [13] Maggiore, M., and Consolini, L., 2013. "Virtual holonomic constraints for euler–lagrange systems". *IEEE Trans. Automat. Contr.*, **58**(4), pp. 1001–1008.
- [14] Chevallereau, C., Grizzle, J. W., and Shih, C.-L., 2009. "Asymptotically stable walking of a five-link underactuated 3-D bipedal robot". *IEEE Trans. Robotics*, **25**(1), pp. 37–50.
- [15] Fantoni, I., Lozano, R., and Spong, M., 2000. "Energy based control of pendubot". *IEEE Trans. Automat. Contr.*, **45**(4), pp. 725–729.
- [16] Xin, X., and Kaneda, M., 2005. "Analysis of the energy-based control for swinging up two pendulums". *IEEE Trans. Automat. Contr.*, **50**(5), pp. 679–684.
- [17] Getz, N., 1995. "Dynamic inversion of nonlinear maps with applications to nonlinear control and robotics". PhD thesis, Dept. Electr. Eng. and Comp. Sci., Univ. Calif., Berkeley, CA.
- [18] Lederer, A., Yang, Z., Jiao, J., and Hirche, S., 2023.

- “Cooperative control of uncertain multiagent systems via distributed gaussian processes”. *IEEE Trans. Automat. Contr.*, **68**(5), pp. 3091–3098.
- [19] Beckers, T., and Hirche, S., 2022. “Prediction with approximated Gaussian process dynamical models”. *IEEE Trans. Automat. Contr.*, **67**(12), pp. 6460–6473.
- [20] Deisenroth, M., and Ng, J. W., 2015. “Distributed gaussian processes”. In Proc. 32nd Int. Conf. Machine Learning, F. Bach and D. Blei, eds., Vol. 37, PMLR, pp. 1481–1490.
- [21] Helwa, M. K., Heins, A., and Schoellig, A. P., 2019. “Provably robust learning-based approach for high-accuracy tracking control of lagrangian systems”. *IEEE Robot. Automat. Lett.*, **4**(2), pp. 1587–1594.
- [22] Chen, K., Yi, J., and Liu, T., 2017. “Learning-based modeling and control of underactuated balance robotic systems”. In Proc. IEEE Conf. Automat. Sci. Eng., pp. 1118–1123.
- [23] Chen, K., Yi, J., and Song, D., 2019. “Gaussian processes model-based control of underactuated balance robots”. In Proc. IEEE Int. Conf. Robot. Autom., pp. 4458–4464.
- [24] Han, F., and Yi, J., 2023. “Gaussian process-enhanced, external and internal convertible (EIC) form-based control of underactuated balance robots”. *arXiv preprint*, pp. 1–7. arXiv:2309.15784. Available at <https://arxiv.org/abs/2309.15784>.
- [25] Wang, P., Han, F., and Yi, J., 2023. “Gyroscopic balancer-enhanced motion control of an autonomous bikebot”. *ASME J. Dyn. Syst., Meas., Control*, **145**(5), article 101002.
- [26] Srinivas, N., Krause, A., Kakade, S. M., and Seeger, M. W., 2012. “Information-theoretic regret bounds for gaussian process optimization in the bandit setting”. *IEEE Trans. Inform. Theory*, **58**(5), pp. 3250–3265.
- [27] Apkarian, J., Karam, P., and Levis, M., 2011. *Instructor Workbook: Inverted Pendulum Experiment for Matlab/Simulink Users*. Quanser Inc., Markham, Ontario, Canada.